Oblique Propagation and Refraction of Gravity Waves Over the Andes Observed by GLORIA and ALIMA During the SouthTRAC Campaign

L. Krasauskas[1] , B. Kaifler[2] , S. Rhode[1] , J. Ungermann[1,3] , W. Woiwode[4] , and P. Preusse[1]

[1]Forschungszentrum Jülich, Institute of Energy- and Climate Research, Stratosphere (IEK-7), Jülich, Germany, [2]Deutsches Zentrum für Luft- und Raumfahrt, Institut für Physik der Atmosphäre, Oberpfaffenhofen, Germany, [3]JARA, Forschungszentrum Jülich GmbH, Jülich, Germany, [4]Karlsruhe Institute of Technology, Institute of Meteorology and Climate Research, Karlsruhe, Germany

Abstract Gravity waves (GW) carry energy and momentum from the troposphere to the middle atmosphere and have a strong influence on the circulation there. Global atmospheric models cannot fully resolve GWs, and therefore rely on highly simplified GW parametrizations that, among other limitations, account for vertical wave propagation only and neglect refraction. This is a major source of uncertainty in models, and leads to well-known problems, such as the late break-up of polar vortex due to the "missing" GW drag around 60°S. To investigate these phenomena, GW observations over Southern Andes were performed during SouthTRAC aircraft campaign. This paper presents measurements from a SouthTRAC flight on 21 September 2019, including 3-D tomographic temperature data of the infrared limb imager GLORIA (8–15 km altitude) and temperature profiles of the ALIMA lidar (20–80 km altitude). GLORIA observations revealed multiple overlapping waves of different wavelengths. 3-D wave vectors were determined from the GLORIA data and used to initialize a GW ray-tracer. The ray-traced GW parameters were compared with ALIMA observations, showing good agreement between the instruments and direct evidence of oblique (partly meridional) GW propagation. ALIMA data analysis confirmed that most waves at 25–40 km altitudes were indeed orographic GWs, including waves seemingly upstream of the Andes. We directly observed horizontal GW refraction, which has not been achieved before SouthTRAC. Refraction and oblique propagation caused significant meridional transport of horizontal momentum as well as horizontal momentum exchange between waves and the background flow all along the wave paths, not just in wave excitation and breaking regions.

Plain Language Summary Gravity waves (GW) are temperature and wind disturbances in the atmosphere that carry energy and momentum from troposphere to the middle atmosphere and have a strong influence on the circulation there. Global atmospheric models currently cannot adequately represent GW propagation: the facts that GWs can change wavefront orientation (refraction) and travel horizontally (and not just vertically) are typically neglected. This leads to important known model inaccuracies, for example, too low temperatures in southern polar regions. SouthTRAC aircraft measurement campaign observed GWs exited by wind flow over the Southern Andes in September–November 2019. Temperature measurements were conducted with the IR spectrometer GLORIA (provided 3-D data) and the ALIMA lidar instrument. GLORIA data revealed many overlapping waves of different wavelengths, their propagation further up was investigated using ray-tracing. Most waves seen by GLORIA were ray-traced to ALIMA observations where their parameters were confirmed, thus validating our ray-tracing technique and the two instruments against each other. We directly observed wave propagation in both vertical and horizontal directions and change in horizontal wave orientation (the latter was not seen before SouthTRAC). Due to these phenomena, many GWs carried momentum that had different directions and was deposited in a different location than most models typically predict.

1. Introduction

Atmospheric gravity waves (GWs) are wind and air temperature perturbations for which gravity acts as the main restoring force (Fritts & Alexander, 2003). They are one of the main mechanisms of energy and momentum transport from the troposphere to the middle atmosphere and hence play a key role in middle atmosphere dynamics (Fritts & Alexander, 2003; Holton & Alexander, 2000). GWs contribute to driving the Brewer-Dobson circulation (Alexander & Rosenlof, 2003) and the quasi-biennial oscillation (Dunkerton, 1997; Ern et al., 2014), have

an influence on the polar vortex (O'Sullivan & Dunkerton, 1995) and sudden stratospheric warmings (SSWs, Ern et al., 2016; Thurairajah & Cullens, 2022) and can cause reversals of zonal mean jets in the mesosphere (Garcia & Solomon, 1985; McLandress, 1998) and effect lower thermosphere through secondary wave emission (e.g., Becker & Vadas, 2018). GW-induced drag also has an impact on the jet stream (Ern et al., 2016; Palmer et al., 1986), convection (de Groot-Hedlin et al., 2017; de la Torre et al., 2011; Koch & Siedlarz, 1999) and tropospheric weather systems (Kidston et al., 2015), and hence influence surface weather.

The most important GW sources include wind interaction with orography (e.g., Eckermann & Preusse, 1999; Nastrom et al., 1987), convection (e.g., Jiang et al., 2004; Sato, 1993), atmospheric fronts (Fovell et al., 1992; Ralph et al., 1999) and unstable jets (e.g., Bühler, 1999; Geldenhuys et al., 2021; O'Sullivan & Dunkerton, 1995; Plougonven & Zhang, 2014). Although conceptual models have been developed to understand and parametrize how these processes can emit GWs (e.g., Charron & Manzini, 2002; Y. H. Kim et al., 2013; Lott & Miller, 1997), there is still a large uncertainty in the amount of gravity wave momentum flux (GWMF) emitted and there are tuning parameters for emission efficiency and scales (e.g., Y.-J. Kim et al., 2003; Scinocca et al., 2008). Therefore one cannot deduce the relative strengths of various sources and their importance for the driving of the circulation in a straightforward way.

GW parametrizations are required because global circulation models (GCMs) and especially chemistry-climate models (CCMs) of the atmosphere cannot resolve significant parts of GW spectrum due to the prohibitive computational cost and rely on highly simplified parametrizations to account for GW activity. These parametrizations cannot accurately represent the spectrum, orientation, or intermittency of the emitted GWs (e.g., Alexander & Dunkerton, 1999; de la Camara et al., 2014; McLandress, 1998; Scinocca & McFarlane, 2000), and typically assume purely vertical GW propagation, even though oblique GW propagation has been shown to occur by observations (Krisch et al., 2017; Sato et al., 2003), by statistical analysis of GW patterns (Choi et al., 2009; Jiang et al., 2004) and with modeling studies (Kalisch et al., 2014; Preusse et al., 2009; Sato et al., 2009). This can cause serious problems in the models. An example relevant to this study is the late break-up of the SH polar vortex ("cold-pole bias problem"; Butchart et al., 2011) present in most CCMs. It is widely believed to be caused by missing GW-induced drag around 60°S in GW parametrizations (e.g., McLandress et al., 2012), several different explanations involving orographic (e.g., Garcia et al., 2017) and non-orographic (e.g., Polichtchouk et al., 2018) sources were suggested and no consensus has been reached. More detailed, source-specific parametrizations have been proposed, but better observational data will be needed to constrain them (Plougonven et al., 2020).

Understanding the origins of observed GWs and attributing them to different sources and source locations is one way to better constrain GW modeling. However, this is still a difficult and rarely undertaken task (Geldenhuys et al., 2021; Hertzog et al., 2008; Pramitha et al., 2015; Wrasse et al., 2006), because it requires full characterization of individual GWs, which cannot be accomplished by most observation techniques. Near-global coverage is provided by satellite instruments, but only nadir-viewing instruments were so far capable of delivering 3-D data products (AIRS; Ern et al., 2017; Hindley et al., 2020; Hoffmann & Alexander, 2009). As they have poor vertical resolution they can detect only the long-wave part of the GW spectrum (larger than around 10–15 km vertical wavelength for AIRS, e.g., Hindley et al., 2019), which corresponds to very high intrinsic phase speed. Detectability of GWs hence depends largely on the background wind speeds. Despite such shortcomings, backward ray-tracing could be employed to infer orographic sources for GWs detected in the southern winter hemisphere (Perrett et al., 2021) and for mesoscale GWs emitted by the Hunga-Tonga eruption (Ern et al., 2022). Current limb-viewing satellites have excellent vertical resolution, but poor resolution along the line of sight (SABER: Russell et al., 1999; HIRLDS: Gille et al., 2003) and no across-track dimension. Therefore the propagation direction cannot be inferred and backward ray-tracing cannot be applied. Only forward modeling studies that make assumptions about source distributions and investigate propagation are possible (Choi et al., 2009; Ern et al., 2006; Preusse et al., 2009; Trinh et al., 2016). New limb-viewing satellites that could provide tomographic 3-D temperature have been proposed (see Ungermann, Hoffmann, et al., 2010 for general discussion, the ESA Earth Explorer 11 candidate CAIRT is a currently proposed satellite with these capabilities), their data would be similar in nature (although of lower resolution) to the 3-D temperature data we present in this work, but have wider altitude range (5–120 km for CAIRT) and be near-global. Full characterization of the wave structure over a limited set of locations in the MLT region can also be achieved using ground-based radar (MAARSY; Stober et al., 2013) or combinations of lidar and airglow measurements (e.g., Cao et al., 2016; Lu et al., 2015). A wave can also be fully characterized, if, for instance, the horizontal wave vector and the phase speed are known. This was used in the back-tracing studies of Pramitha et al. (2015) and Wrasse et al. (2006). Finally, the full 3-D wave

vector can also be obtained using wind measurements from in situ instruments in radiosondes (e.g., Vincent & Alexander, 2000), superpressure balloons (Hertzog et al., 2008; Podglajen et al., 2016) and aircraft (e.g., Smith et al., 2016; Wagner et al., 2017), or from ground-based wind radar (PANSY; Minamihara et al., 2020). These wind measurements can be used to trace waves to their sources, but they have very limited spatial coverage. Generally, trajectory calculations are sensitive to small perturbations of the starting conditions. Their behavior can be influenced by uncertainties of the atmospheric background conditions as well as the determination of the initial wave vector from the observations. In general, the GW source determination is most reliable at relatively low altitudes, for example, in the lower stratosphere, and for waves that propagate steeply. More complex processes along the path of the ray, such as strongly oblique propagation and horizontal refraction (discussed in the following paragraph), enhance uncertainties. While successful back-tracing studies are reported, ray-traced waves were not previously observed at multiple locations along the raypath in order to validate the technique as such.

Horizontal refraction describes the change of the horizontal wave vector, which occurs as the wave propagates through horizontal wind gradients and is another often neglected aspect of wave propagation. This phenomenon can be predicted and quantified from the point of view of linear wave theory (Holton, 2004; Marks & Eckermann, 1995), previous studies used GW-permitting models (Chen et al., 2005; Hasha et al., 2008) or combined these models with ray-tracing (Strube et al., 2021). Due to the lack of observations that would allow us to infer the wave propagation direction at multiple altitudes, no direct observational confirmation of horizontal refraction was achieved before the SouthTRAC (Southern Hemisphere Transport, Dynamics, and Chemistry) measurement campaign (Geldenhuys et al., 2022, and this work). Despite this lack of observational evidence, substantial impact on the interaction of GWs with the background flow is expected: by changing the horizontal wave vector, horizontal refraction alters the amount and direction of the horizontal momentum carried by the wave and can hence result in a significant redistribution of momentum along the path of wave propagation. This phenomenon is also mostly ignored in current GW parametrizations. Refraction also alters the overall direction of wave propagation and is therefore important for understanding oblique propagation in general. In order to validate these general theoretical concepts and motivate their application in global modeling approaches, we need an observational study, where all these aspects govern wave propagation and hence the distribution of the observed GW field.

In order to obtain observations of the same waves at various altitudes and to fully characterize the waves allowing ray-tracing, two highly innovative instruments were deployed on the High Altitude LOng range research aircraft of the German research community for the SouthTRAC measurement campaign. The Gimbaled Limb Observer for Radiance Imaging of the Atmosphere (GLORIA; Friedl-Vallon et al., 2014) is an airborne IR limb imager with the unique capability to provide high-resolution 3-D temperature and trace gas data by observing an air mass from multiple directions and performing a 3-D tomographic retrieval, and is therefore ideally suited for in-depth analysis of GWs in the upper troposphere – lower stratosphere (UTLS). GLORIA has been successfully used for GW (Krisch et al., 2017) and trace gas (Krasauskas et al., 2021) observations in the UTLS region. The second instrument is the Airborne LIdar for Middle Atmosphere research (ALIMA, see Section 2.2), which provides temperature data above the aircraft between the altitudes of 20 and 80 km and thus shows how the waves observed by GLORIA propagate into the middle atmosphere. The SouthTRAC campaign was based in Rio Grande, Patagonia, and several research flights were dedicated to the observation of oblique wave propagation and horizontal refraction.

In this paper, we present GW observations from a research flight over the Southern Andes, which were conducted on 20–21 September 2019 as part of the SouthTRAC measurement campaign (Rapp et al., 2021). On the day of the flight, SW wind over the Andes caused high amplitude orographic GW activity, which was observed using GLORIA 3-D tomography and ALIMA data. Our general strategy for data analysis was as follows:

1. Use the S3D small-volume wave-fitting code to identify GWs in the GLORIA data and determine their main parameters (wave numbers and amplitudes).
2. Use these wave parameters to initialize the GROGRAT ray tracer and trace way propagation upwards.
3. Since most of these rays propagated through the regions observed by the ALIMA instrument, compare the wave parameters of the GLORIA-data-initialized rays to those obtained from the ALIMA observations. This validates our ray-tracing approach and provides an opportunity to compare the data from two instruments that observed different altitudes

Table 1
Spectral Windows for GLORIA 3-D Temperature Retrieval

#	Spectral range, cm^{-1}	#	Spectral range, cm^{-1}
1	791.0–793.0	6	980.0–984.2
2	863.0–866.0	7	992.6–997.4
3	892.6–896.2	8	1,000.6–10,006.2
4	900.0–903.0	9	1,010.0–1,014.2
5	956.8–962.4		

4. Use the validated ray-tracing results to study different aspects of wave propagation, such as horizontal refraction and apparent wave propagation to the upwind side of the Andes.

5. Directly compare ALIMA data to ECMWF operational analysis and the newly developed simple mountain wave model (MWM).

Section 2 briefly describes the GLORIA and ALIMA instruments, their temperature retrieval techniques, our wave parameter fitting code (S3D), and the GROGRAT ray tracer that were used for data analysis, as well as ECMWF data used for model comparisons. MWM is introduced at the end of the section. Section 3 presents the results and is subdivided as follows. Section 3.1 describes the meteorological conditions during observation. Section 3.2 presents GLORIA temperature data. Section 3.3 describes how wave parameters were obtained from GLORIA data and discusses wave origins. Section 3.4 describes ray-tracing results and compares them to ALIMA measurements. The propagation of the shortest waves detected by GLORIA is discussed separately in Section 3.5. The most interesting aspects of GW propagation over the Andes are then analyzed in Section 3.6 using results from both instruments. Section 3.7 presents MWM results, as well as ECMWF, MWM, and measurement data comparisons. Finally, conclusions are given in Section 4.

2. Data and Methods

2.1. The GLORIA Instrument and Retrievals

The GLORIA is an airborne IR limb imaging spectrometer. It records spectra in the 770–1,400 cm^{-1} wave number range (Friedl-Vallon et al., 2014; Riese et al., 2005). In the applied configuration, GLORIA uses 128×48 effective pixels out of a 256×256 pixel detector array. GLORIA has a 1.5° field of view in the horizontal direction and 4° field of view in the vertical (typically −3° to 1° elevation above the horizon). Infrared radiation along any line of sight comes mostly from the lowest point on the line of sight (called *tangent point*). Therefore, different line-of-sight elevations result in very different tangent point altitudes, allowing for very high vertical resolution of up to 200 m of the retrieved atmospheric quantities and a wide altitude range. The lower limit of observable altitude is around 5 km (due to clouds, aerosols, strong continuum emissions of water vapor below), and the upper limit is the flight altitude of the carrier aircraft (up to 15 km for the HALO aircraft used for this study).

GLORIA is a versatile instrument that can be used to observe air temperature and mixing ratios of multiple trace gases. In this paper, we will only consider 3-D tomographic temperature data used for studying GWs. For this type of measurement, we use a short interferogram scan with a spectral sampling of 0.2 cm^{-1} and an acquisition time of ≈5 s. This is sufficiently fast for instrument panning, that is, alternating the observation direction with respect to aircraft heading between 11 values in the 45°–135° range. Panning allows to observe the same air mass from multiple directions, hence 3-D tomography is possible even using observations from a single straight flight leg, but such tomographic retrievals have lower resolution in the horizontal direction perpendicular to the flight track (Krisch et al., 2018, 2020). For the best resolution in every direction, the aircraft needs to be flown around the observed air mass in a close-to-circular flight pattern with a diameter of around 200 km and also panning the instrument. Due to practical considerations, the actual tomography-optimized flight paths are typically hexagonal and around 400 km in diameter (Ungermann, Hoffmann, et al., 2010).

3-D retrievals are performed by means of inverse modeling, using the Jülich Rapid Spectral Simulation Code Version 2 (JURASSIC2). The radiative transfer model (Hoffmann et al., 2008) employed as the forward model uses the emissivity growth approximation method (Gordley & Russell, 1981; Weinreb & Neuendorffer, 1973) and the Curtis-Godson approximation (Curtis, 1952; Godson, 1953). A Newton-type trust region algorithm (Marquardt, 1963) and a conjugate gradients solver (Hestenes & Stiefel, 1952) are used for inverse modeling. Calculations were performed on an irregular grid with a Delaunay triangulation, using a Laplacian-based regularization technique with physical parameters (Krasauskas et al., 2019). For more information about the 3-D tomography implementation refer to Krasauskas et al. (2019), Ungermann, Kaufmann, et al. (2010), and Ungermann et al. (2011).

The temperature retrievals presented in this paper were performed using radiances from the spectral windows given in Table 1.

The retrieval also requires additional temperature and trace gas volume mixing ratio (VMR) data (called a priori data). It is needed to account for the IR radiation that various trace gases contribute to GLORIA observations and for retrieval regularization (Krasauskas et al., 2019). GLORIA temperature data is not strongly affected by uncertainties in trace gas VMRs, as it relies heavily on IR emissions of CO_2, which is well-mixed in the atmosphere and has low uncertainties in its VMR. The a priori data for air temperature and pressure was taken from the European Center for Medium-Range Weather Forecasts (ECMWFs; Dee et al., 2011) operational analysis (T1279/L137 resolution). Whole Atmosphere Community Climate Model (e.g., Garcia et al., 2007) data was chosen as a priori for O_3 and HNO_3. Since a priori data must be smooth (i.e., have no sharp transitions), reflect large-scale features of the relevant physical quantities, and do not contain any perturbations due to GWs, a low-pass filter (Savitzky & Golay, 1964) was applied to all a priori data sets.

2.2. The ALIMA Instrument

The ALIMA as flown during SouthTRAC is a compact upward pointing Rayleigh back-scatter lidar. It uses a frequency-doubled pulsed neodymium-doped yttrium aluminum garnet (Nd:YAG) laser with a mean optical output power of 12.5 W and 125 mJ pulse energy at 532 nm wavelength as light source. Back-scattered light is collected using a fiber-coupled 48 cm diameter Cassegrain telescope with a field of view of 330 μrad during lidar operation in darkness and 165 μrad in daylight. A set of three cascaded single-photon counting detectors covers the full dynamic range of the lidar return signal starting at about 5 km above the aircraft flight level to approximately 90 km altitude. In addition to reducing the telescope field of view, narrow-band optical filters (etalons) can be inserted in the receiver for enhanced rejection of the strong solar background when the lidar is operated in daylight.

Temperature profiles are retrieved by hydrostatic integration of the lidar back-scatter profiles in a similar way as for the ground-based CORAL instrument (Kaifler & Kaifler, 2021) at a cadence of one profile every 2 min, which corresponds to a horizontal resolution of 26 km assuming an aircraft speed of 220 m/s. The vertical resolution of the temperature profiles used in this study is 1,500 m. For this 2 min × 1,500 m resolution data set, typical uncertainties of the retrieved temperatures are 2.1 K within the altitude range of 30–40 km and increase to 6.8 K in the 60–70 km range.

In this work, the ALIMA data are presented in the form of 2-D curtains of different flight legs and wavelet spectra. The curtains were detrended by computing the mean temperature profile (i.e., temperature as a function of altitude) for the whole flight leg, applying a low-pass filter (Savitzky-Golay filter of order 3 with window width of 51 points (5 km), Savitzky & Golay, 1964) to the profile and subtracting the result from the temperature data. The resulting detrended temperature was used to compute the ALIMA GW spectrum, that is, the spectrum of atmospheric GWs projected onto the vertical plane of ALIMA observations. Continuous 2-D Morlet wavelet decomposition (Morlet et al., 1982; Torrence & Compo, 1998) was employed. This method technically yields a 2-D GW spectrum for each grid point on the ALIMA curtain. The short-wavelength components of such a spectrum depend only on the temperature residuals close to that grid point, while the spectral components corresponding to longer waves are also influenced by temperature structures further away. Aspect ratio (i.e., ratio between horizontal and vertical spatial sampling for spectral analysis) was set to 40 to conform with the mean of the typical ratios between horizontal and vertical GW wavelengths (e.g., Figure 5), 48 scales and 54 uniformly distributed wavelet orientations were used. We will also discuss a GW spectra in specific regions of ALIMA observations (the regions will be shown in figures), which will be defined as the mean of the Morlet wavelet spectra for each point in the region. This way, a GW spectrum for wavelengths shorter than the region dimensions is defined almost entirely by the data within the region, while spectral components corresponding to longer wavelengths depend also on the data from region's surroundings.

Note also that since ALIMA data is presented as a set of vertical cuts through the atmosphere, the apparent horizontal wavelength in ALIMA data λ_{ha} is not the same as the actual horizontal wavelength. In fact $\lambda_{ha} = \lambda_h / \cos \alpha$, where α is the angle between the ALIMA curtain and the horizontal wave vector. This is because λ_{ha} corresponds to the projection of horizontal wave vector onto the ALIMA curtain. This fact was, naturally, taken into account when comparing ALIMA data to GLORIA-data-initialized ray traces.

2.3. S3D Wave Parameter Fitting Code

GW parameters (wave vector **k** and amplitudes) were determined from GLORIA 3-D temperature data using a small-volume few-wave decomposition method S3D (Lehmann et al., 2012), implemented as part of the JUWAVE

Table 2
S3D Wave Fitting Box Parameters

S3D run	A	B
Horizontal extent, km	300×300	100×100
Horizontal extent, GLORIA grid	25×25	9×9
Horizontal wavelength range, km	100–900	50–150
Vertical extent, km	3.5	3.5
Vertical extent, GLORIA grid	29	29
Vertical wavelength range, km	1.2–10.5	1.2–10.5

GW analysis software package developed in Forschungszentrum Jülich. As a first step, GLORIA temperature data was detrended using Savitzky-Golay low-pass filter (Savitzky & Golay, 1964), to separate the temperature disturbances due to GWs (wavelengths lower than approximately 800 km) from the background. The main idea of the method is to subdivide the measurement volume into smaller regions (rectangular boxes) and perform a least squares fit on the detrended temperature data in each box, by minimizing

$$\chi^2 = \sum_i \left(T_i - \sum_{j=1}^{n} \left[A_j \sin\left(\mathbf{k}_j \cdot \mathbf{x}_i\right) + B_j \cos\left(\mathbf{k}_j \cdot \mathbf{x}_i\right) \right] \right), \quad (1)$$

where $\mathbf{x}_i$ and T_i are measurement data point positions and the respective residual temperature values at those points. In general, n different waves can be fitted with $j = 1, \ldots, n$, $\mathbf{k}_j$ are the wave vectors, and A_j, B_j are amplitudes of the wave components of different phases. The temperature amplitude of the j'th wave is then $T_{aj} = \sqrt{A_j^2 + B_j^2}$. The optimal $\mathbf{k}_1$ is found using variational methods, then A_1, B_1 are determined analytically. When fitting more than one wave ($n > 1$), we determine the parameters of the j'th wave by subtracting the $j - 1$ waves that were already fitted from the temperature field first, and then proceeding in the same way as for the first wave. In the studies described in this paper, two waves were fitted for each fitting box ($n = 2$). This accounts for the possibility of overlapping wave patterns in the same volume.

S3D was chosen for this work over the more common Fast Fourier Transform (FFT) or wavelet methods, because it works well for small volumes of data and is not limited by a set of discrete frequencies. It has been shown (Lehmann et al., 2012; Preusse et al., 2012) to reliably determine wavelengths that range from one third to three times the size of the rectangular box in the corresponding dimension. Such capability is needed, since the vertical wavelengths of many GWs discussed in this paper are actually larger than the useable vertical extent of GLORIA 3-D data, and the longest horizontal wavelengths span the whole 3-D tomography hexagon.

In this study, GWs with horizontal wavelengths $\lambda_h > 500$ km could be clearly seen in GLORIA data (Section 2.1), and short waves with $\lambda_h < 65$ km were also expected (see the beginning of Section 3.3). The limitations of S3D outlined above do not allow to reliably resolve such a large wavelength range using a single box size. Therefore, two separate S3D runs (A and B) were used. The sizes of the retrieval boxes used in each run are given in Table 2, together with the ranges of GW wavelengths that could be reliably retrieved from each run. The main analysis was performed using run A, the results of this analysis are presented in Section 3.3 and used for subsequent analysis throughout the paper. S3D run B was intended specifically for detecting short waves with $\lambda_h < 100$ km that would have been missed by the first run. To that end, an additional high-pass filter was applied to remove waves with $\lambda_h > 150$ km. Due to the limits of GLORIA's horizontal resolution, we can in principle expect to see waves with $50 \text{ km} < \lambda_h < 150 \text{ km}$ for run B. The analysis of these short waves is presented in Section 3.5. We used a total of 169 fitting boxes for both runs. The fitting boxes were centered at 11 km altitude, so that the box spanned the altitudes from 9.25 to 12.75 km. In the horizontal direction, box centers formed a 13×13 square grid, the center of this grid coincided with the center of the hexagon. The spacing of this grid was 12.5 km, equal to the GLORIA data horizontal spacing. Two examples of the fitting boxes (one large from run A, and one small from run B) are shown in Figure 2d.

2.4. The GROGRAT Ray-Tracer

The Gravity wave Regional or Global RAy Tracer (GROGRAT; Marks & Eckermann, 1995) was used for ray-tracing the GWs observed by GLORIA and as part of the MWM described in Section 2.5. The basics of GROGRAT operation can be described as follows. Let $\mathbf{x} = (x, y, z)$ and $\mathbf{k} = (k, l, m)$ be the position and wave vector of a GW packet, respectively. Then, denoting $\partial_{\mathbf{a}} \equiv (\partial/\partial a_x, \partial/\partial a_y, \partial/\partial a_z)$ for any vector $\mathbf{a} = (a_x, a_y, a_z)$, the ray-tracing equations (Lighthill, 1978) can be written as follows:

$$\frac{d\mathbf{x}}{dt} = \partial_{\mathbf{k}}\omega \qquad \frac{d\mathbf{k}}{dt} = -\partial_{\mathbf{x}}\omega, \quad (2)$$

where ω is the ground-based frequency, which GROGRAT determines from the GW dispersion relation

$$(\omega - Uk - Vl)^2 = \frac{N^2(k^2 + l^2) + f^2(m^2 + \alpha^2)}{k^2 + l^2 + m^2 + \alpha^2}. \tag{3}$$

Here $(U, V, 0)$ is the background wind, f—Coriolis parameter, N—Brunt-Väisälä frequency, and $\alpha \equiv 1/2H$, where H is the density scale height of the atmosphere. N and α are calculated from the temperature background, which, along with the horizontal winds U, V, is obtained from smoothed-out ECMWF operational analysis data. The background data are processed in the same way as GLORIA a priori (see description in Section 2.1). Then, given the observed wave location **x** and wave vector **k**, these quantities are calculated forwards and backward in time. The evolution of GW amplitude along the ray path is obtained assuming the conservation of wave action flux, dissipation by turbulent and radiative damping, and dissipation by saturation (for details, see Andrews et al., 1987; Marks & Eckermann, 1995). The ray-tracing approximations remain valid as long as the Wentzel-Kramers-Brillouin approximation (WKB; Einaudi & Hines, 1970) holds. The latter condition ensures that relevant parameters of the background change sufficiently slowly in space and time. A violation of WKB would usually indicate a level where partial reflection occurs. Rays are terminated once the corresponding GWs reach a critical level, break down in amplitude or reach the altitude of 70 km.

Within GROGRAT, GW amplitudes are given as the amplitudes of horizontal wind perturbation due to the waves. Since we will only be dealing with temperature measurements in this work, all GW amplitudes will be discussed in terms of amplitudes of the temperature perturbation. These two different types of amplitudes are related. Using linear GW theory (e.g., Fritts & Alexander, 2003), and all assumptions being consistent with the ones used in GROGRAT and outlined above,

$$\left(u_a^2 + v_a^2\right)\left[1 - \left(\frac{f}{\hat{\omega}}\right)^2\right] = \left(\frac{g}{N}\right)^2\left(\frac{T_a}{T_0}\right)^2, \tag{4}$$

where u_a, v_a, and T_a are the amplitudes of zonal wind, meridional wind, and temperature, respectively, and $\hat{\omega} = \omega - Uk - Vl$ is the intrinsic wave frequency, that can be calculated from Equation 3. Equation 4 is used to compute the horizontal wind amplitude $\sqrt{u_a^2 + v_a^2}$ from S3D data (**k** and T_a) when initializing GROGRAT rays from GLORIA measurements, and to compute temperature amplitudes from wind amplitudes in the GROGRAT output.

Another wave parameter calculated by GROGRAT along the raypath is the horizontal gravity wave momentum flux (GWMF) defined as follows:

$$(F_{px}, F_{py}) = \rho\left[1 - \left(\frac{f}{\hat{\omega}}\right)^2\right]\left(\overline{u'w'}, \overline{v'w'}\right). \tag{5}$$

where ρ is air density, and u', v', w' are the perturbations to the wind vector (u, v, w) due to GWs. GWMF represents the momentum that GWs carry from their sources to breaking regions and thus quantifies the effect that GWs have on the mean flow. In this work, we used GWMF data from GROGRAT output (calculated from wind amplitudes and Equation 5), but our assumptions are consistent with the ones in Ern et al. (2015), where linear GW theory and the mid-frequency approximation were used to derive the following expression of GWMF from temperature measurements directly

$$(F_{px}, F_{py}) = \frac{\rho}{2}\left(\frac{g}{N}\right)^2\frac{(k, l)}{m}\left(\frac{T_a}{T_0}\right)^2. \tag{6}$$

2.5. Mountain Wave Model

The MWM estimates orography-induced GW activity based on the topography of the region being investigated. The model is inspired by the algorithm described by Bacmeister (1993) and Bacmeister et al. (1994), but differs in the implementation of the ridge detection method. The calculation of GW distribution at a specific altitude in the atmosphere is implemented as follows. First, topography data is taken from the ETOPO1 1 arc-minute Global Relief Model (Amante & Eakins, 2009; National Geophysical Data Center, 2009), elevation is set to zero where data points are negative to approximate the sea surface. Then the MWM selects scales of interest by applying a
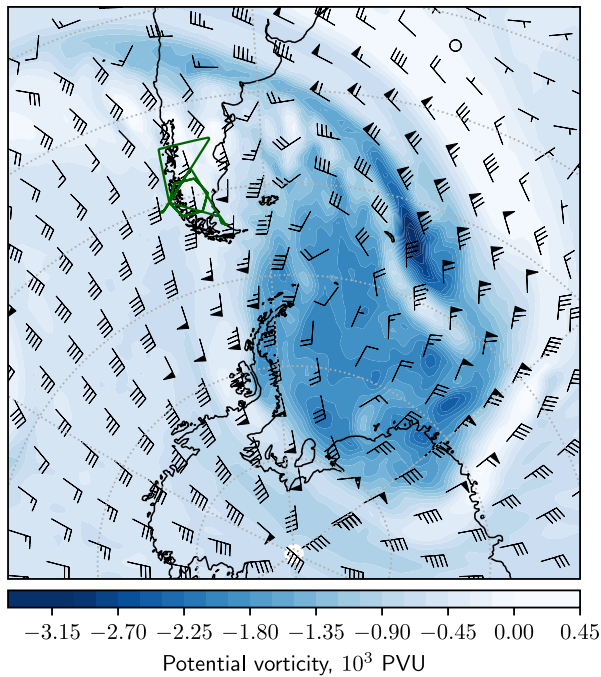
Figure 1. Potential vorticity (PV) and winds for 35 km altitude on 21 September, 06:00 UTC (ECMWF operational analysis). Polar vortex can be identified with highly negative PV values. Wind velocity and direction is indicated by barbs (triangle represents 50 m/s, long barb 10 m/s, short barb 5 m/s).

Gaussian band pass filter to the topography. The filtered topography is further reduced to the arête lines by a gradient method, and straight ridge segments are identified from these by performing a probabilistic Hough transformation (e.g., Shapiro & Stockman, 2001). This provides a collection of lines with their respective positions, lengths, and orientations, which is used for the positions of the mountain ridges. Idealized, Gaussian shaped ridges for these lines are fitted to the band pass filtered topography. In order to determine a GROGRAT ray launch distribution, the horizontal wavelength and displacement amplitude of GWs induced by flow over these idealized ridges are calculated as $\lambda_h = 4.9\sigma$ and $\zeta = h/2$ respectively, with σ being the width and h the height of the best fit Gaussian ridge (elevation $h\exp(-x^2/2\sigma^2)$, where x is the horizontal coordinate). The value of $\lambda_h/\sigma \approx 4.9$ has been estimated from fitting a Gaussian with width σ to a sine of corresponding wavelength λ_h. MWM implements flow blocking by reducing the effective height, and thus the displacement amplitude, of the mountain ridges to $\min(h, h_{\text{eff}})$, with $h_{\text{eff}} = U_{\text{perp}}/(NF_c)$, where the tuning parameter $F_c = 4$ (e.g., van Niekerk & Vosper, 2021). Time development of the mountain waves is predicted by passing the aforementioned GW parameters to the GROGRAT ray tracer and launching the rays hourly for the time period of interest.

The background fields used by the MWM for the ray-tracing are ECMWF ERA5 hourly data (C3S, 2017; Hersbach et al., 2018) with T639/L137 spatial resolution, interpolated to 130 equidistant height levels between 0 and 64.5 km with 0.3° horizontal sampling. A smooth large-scale background was generated as described in Section 3.1.

3. Results and Analysis

3.1. Synoptic Situation and the Measurement Flight on 21 September

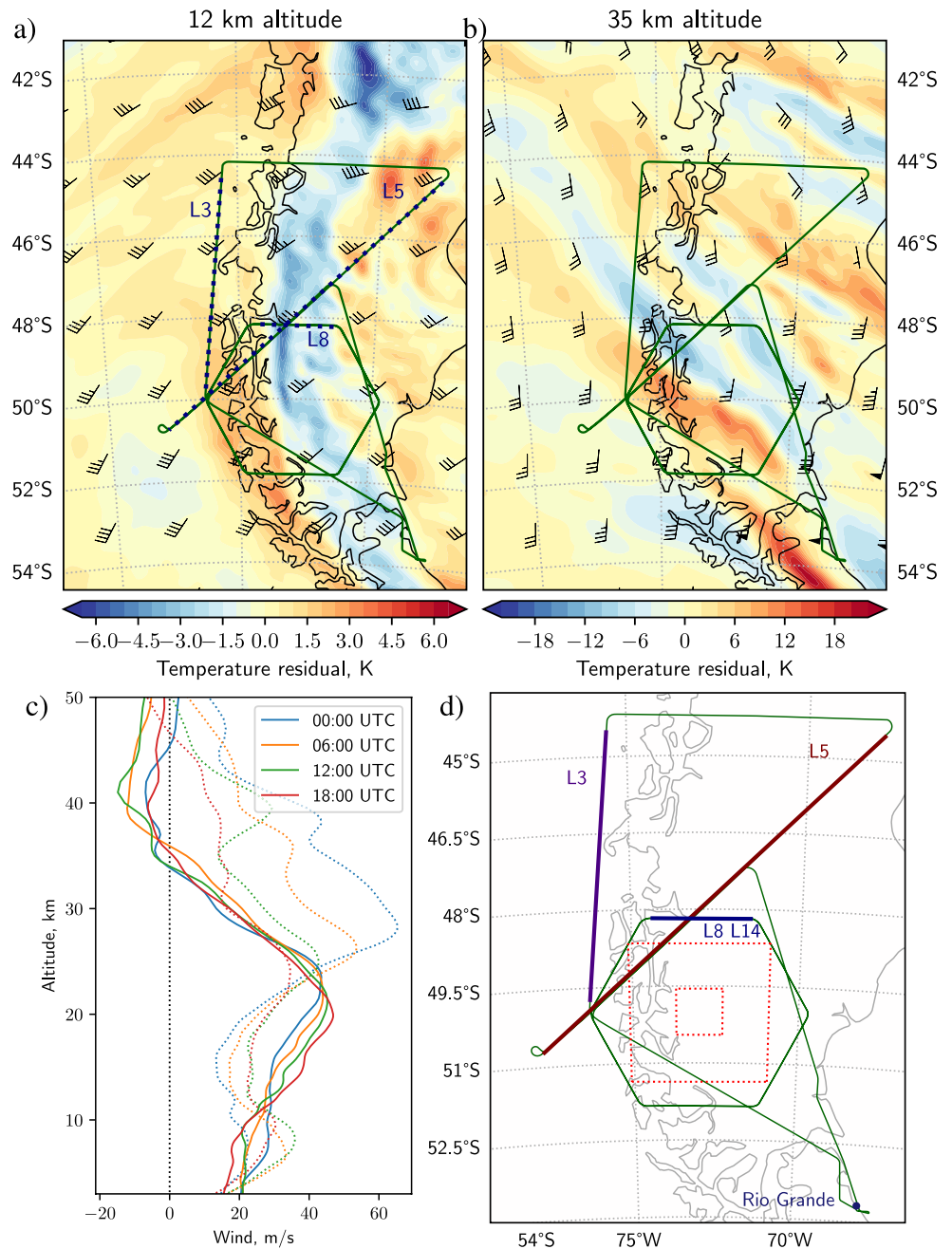The region of Southern Andes is the strongest hotspot of stratospheric GW activity on Earth (Ern et al., 2018; Hindley et al., 2015; Hoffmann et al., 2016). Typical conditions in this region during the austral spring include strong westerly winds from the Pacific interacting with the Andes and causing intense GW excitation. Since the Southern Hemisphere polar vortex is usually more stable than the vortex in the Northern hemisphere, westerly winds typically prevail through most of the middle atmosphere, providing favorable conditions for the aforementioned GWs to propagate upwards all the way to the mesosphere. Studying these waves was one of the main goals of the SouthTRAC measurement campaign. The scientific flights of SouthTRAC dedicated to GWs were conducted 11–26 of September 2019 with the HALO aircraft operating from Rio Grande, Argentina. This coincided with a rare occurrence of a SSW in the Southern Hemisphere, that started in the end of August, with westerly wind velocities at 60°S, 10 hPa level reaching their minimum on 18 September (e.g., Rao et al., 2020), just 3 days before the measurement flight discussed in this paper. In the course of the SSW, the polar vortex was displaced from the pole and passing over the Andes at the time of measurement (Figure 1a). In the troposphere, south-westerly wind reached 30 to 40 m/s and hence excited large-amplitude mountain waves (Figure 2a). However, the wind direction changed significantly with altitude in the stratosphere (Figure 2c), and waves encountered their critical levels at 35–40 km altitude, where zonal wind changed direction. Orographic GWs cannot propagate above zero wind, either caused by a wind reversal or by winds becoming perpendicular to the wave vector.

While this synoptic situation did not allow for observation of GW propagation to the mesosphere with the ALIMA instrument, the complex wind pattern below the critical layer raised interesting questions. Before the measurement flight was executed, ECMWF forecasts showed GWs extending over the Pacific at an altitude of around 35 km, seemingly upwind of the Andes (Figure 2b, west of the coast around 47°S). This raised a question of whether these were indeed orographic GWs, or whether they were excited by some other process. This will be further discussed in Section 3.6.

The flight track of the measurement flight of 21 September is shown in Figure 2a. After take-off from Rio Grande, the HALO aircraft flew to the Pacific coast and observed air masses upwind of the Andes mountain

Figure 2. Panels (a–c) show ECMWF operational analysis for 21 September 2019. Panels (a and b)—detrended temperature (color scale) and wind (barbs) horizontal cuts at 12 and 35 km altitude, respectively, at 06:00 UTC. Wind barbs are defined as in Figure 1a. Green lines indicate HALO flight path. Panel (c)—wind profiles over 50°S 73°W (center of the hexagonal flight pattern). Solid lines indicate zonal wind, dotted lines—meridional wind. Panel (d)—Flight path (green) with important flight legs labeled. L8 and L14 where flown in the same location 90 min apart. Red dots show examples of S3D fitting boxes (large—run A, small—run B).

range (flight segment labeled "L3" and marked by blue dots). The flight path then crossed the mountain range twice, the second crossing (segment "L5") being a long flight leg oriented against the wind at 25 km altitude and providing optimal conditions for ALIMA observations. The rest of the flight was used for encircling a 400 km stretch of the mountain range with a hexagonal flight pattern (Figure 2a, around 50°S 73°W) optimized for GLORIA 3-D tomographic retrieval, before heading back to the airport for landing. The hexagonal flight pattern was performed twice in order to capture temporal development as well. The first and second hexagon were
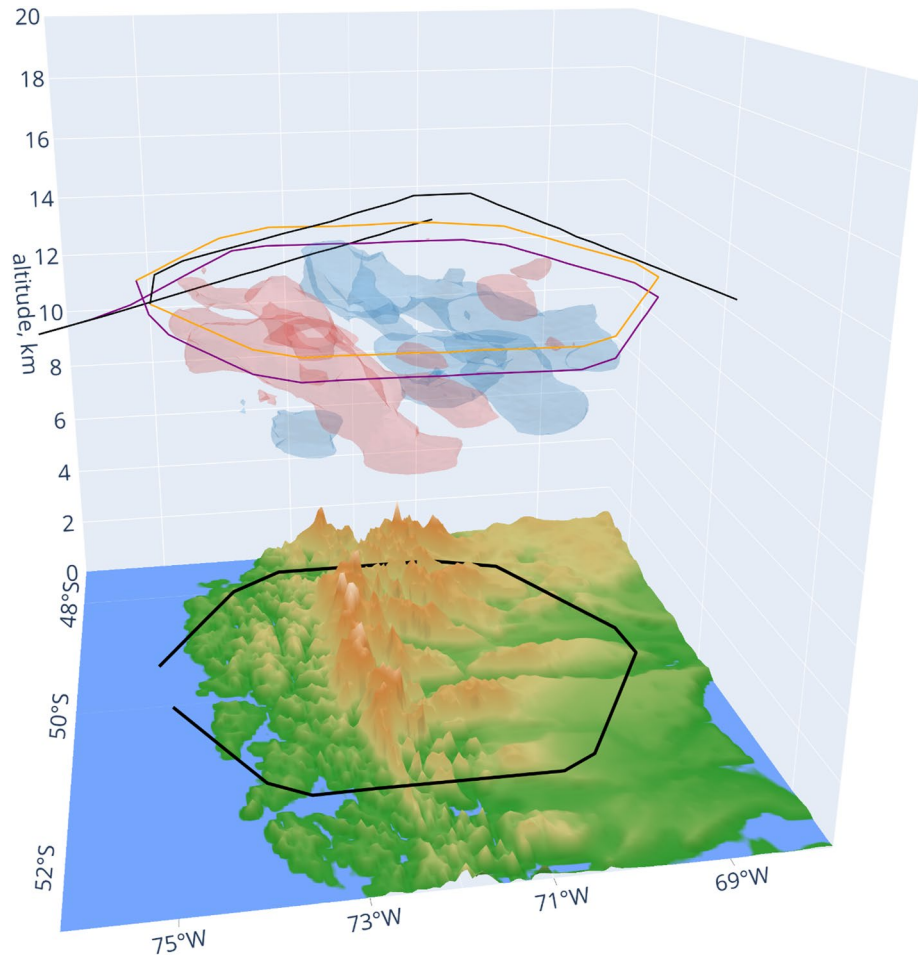
Figure 3. A 3-D visualization of the large-scale temperature structure obtained from GLORIA tomographic retrieval. Blue and red isosurfaces show ±2K residual temperature. The thick black line indicates the ground track of the hexagonal flight pattern. Flight tracks for the first and second hexagons are shown as orange and purple lines, respectively, the rest of the flight within the shown volume is represented by the thin black line.

flown at the (average) altitudes of 12.7 and 13.4 km, respectively. A detailed study of the time dependence of the temperature structures observed by GLORIA is outside the scope of the current paper and subject to further work. This paper focuses on understanding the general structure and propagation characteristics of the observed waves.

3.2. GLORIA 3-D Tomography

The large-scale structure of the GLORIA 3-D tomographic retrieval is presented in Figure 3. More detail can be seen in the 2-D cuts through the retrieval volume (Figure 4). Both figures show the GLORIA temperature data with a high-pass filter (Savitzky-Golay filter of order 3 with window width of 51 points (625 km), Savitzky & Golay, 1964) applied to isolate GWs. The region where the data is valid is roughly funnel-shaped and corresponds to the area covered by the limb sounding tangent points (see Section 2.1). Observations of the first hexagon (left-side panels of Figure 4) are valid at 03:42 UTC, those of the second hexagon (Figure 3 and right-side panels of Figure 4) are valid at 05:22 UTC (these are the time-wise midpoints of each hexagonal pattern, which took about 100 min each to execute). Our measurements reveal highly complex spatial temperature structure. We will identify the most important features and wave groups in the retrieved temperatures in this section, and continue with the more quantitative analysis based on least squares fitting in Section 3.3.

The most prominent structure in the retrieved temperature is the large horizontal wavelength (about 350 km) GW with phase fronts roughly parallel to the South American coastline. It manifests itself with high positive temperature residuals in the eastern side of the hexagon at 10 km altitude, negative temperature anomalies in the
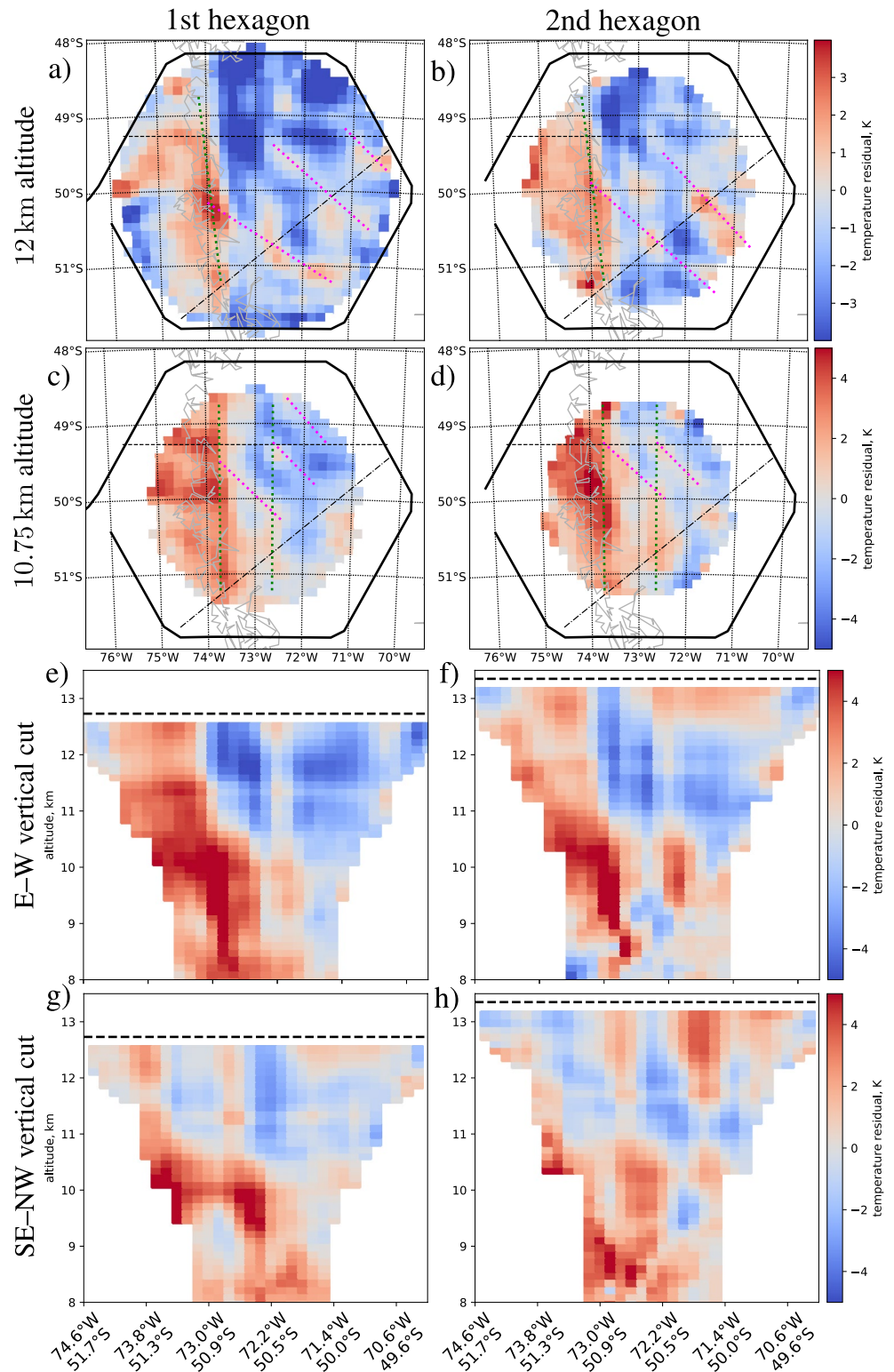
Figure 4. Temperature maps at 12 km altitude (panels (a–b)), maps at 10.75 km altitude (panels (c–d)) and vertical cuts (panels (e–h)) through GLORIA 3-D retrievals. Panels on the left and right present data acquired while flying the first and second hexagons, respectively. The thick solid black line shows the flight path, thick black dashes—flight altitude. Thin black dashes and dash-dots indicate the positions of vertical cuts shown in panels (e–f), and the cuts shown in panels (g–h), respectively. Colored lines mark various waves (see Section 3.2 of the main text).
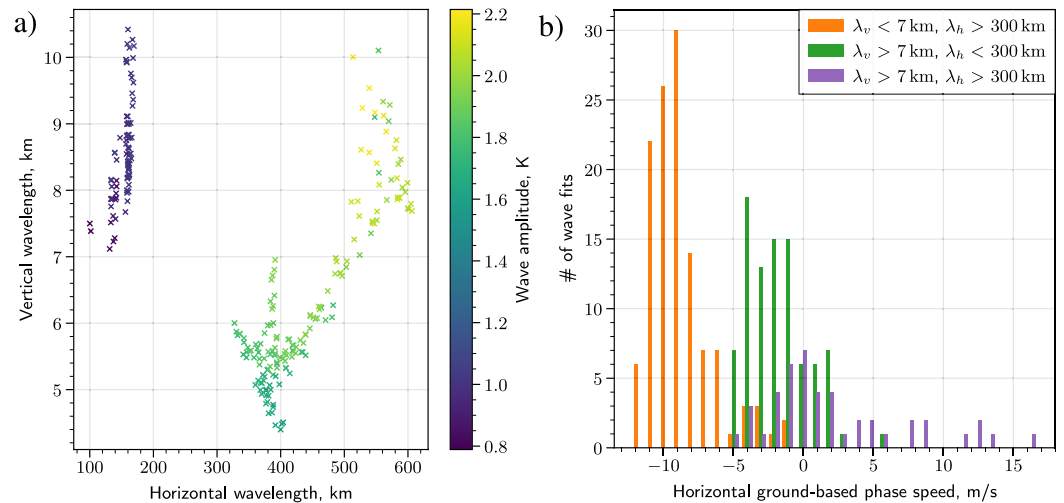
Figure 5. Gravity wave parameters were determined by applying S3D to measurements from the second hexagon. Panel (a)—horizontal and vertical wavelengths (λ_h, λ_z), as well as temperature amplitude (color coded) for each fit. Panel (b)—distribution of fits with respect to ground-based horizontal phase speed. All valid fits fall into one of the three groups defined in the legend.

center (especially between 71.5°W and 73.5°W) and positive temperature residuals on the far eastern edge of the hexagon (the latter especially above 12 km altitude). This long wave accounts for most of the structure seen in Figure 3, and is in good agreement with ECMWF data (Figure 2), which shows a prominent warm-cold-warm feature of very similar length scale along the Andes. There is also a shorter wave (horizontal wavelength around 120 km) of similar orientation, highlighted with green dots in Figures 4c and 4d and clearly seen below 10.5 km altitude in Figure 4f. A slight change in the orientation of these waves with altitude is observed. Below about 11 km, phase fronts are aligned almost exactly in the North-South direction, while at higher altitudes a slight counterclockwise turn occurs (green dotted lines in Figures 4a–4d). This will be discussed in terms of horizontal refraction in Section 3.6.

GLORIA data also reveals a group of waves with phase fronts oriented in approximately NW-SE direction, that is, perpendicular to the wind. These waves have a lower amplitude, but can still be seen in Figure 4 (wavefronts marked with magenta dots in panels (a–d), also seen in panels (g, h)).

Comparing data from the first and second hexagons (Figure 4, panels on the left and right, respectively) reveals some differences in wavefront positions, wave amplitudes, and the smallest scale waves, but no dramatic differences in temperature structure. This shows that the wavefield did not undergo large changes over the period of flying both hexagons, and the instrument was indeed looking into similar structures from different directions during the course of flying each hexagon, that is, the 3-D tomography concept is adequate.

Finally, one must consider the effect of the tropopause on the GW structure in GLORIA data. The buoyancy frequency typically varies sharply with altitude close to the tropopause, and it follows from the dispersion relation (Equation 3) that this leads to rapid changes in the vertical wavelength, leading to a perturbed wave structure around the tropopause and potential partial reflection of GWs (the GWs seen by GLORIA have intrinsic frequency too far from N to make total reflection relevant). The tropopause height inside the hexagonal flight pattern was 8.5–9 km, and one can indeed see the deformed wavefronts below 9 km in Figures 4f and 4h. The tropopause layer was therefore excluded from any wave fitting attempts, all the data about wave parameters was derived from altitudes above 9.25 km.

3.3. Wave Parameter Identification in GLORIA Data and Wave Origins

Our analysis of the GLORIA 3-D data from Section 3.2 identified GWs with a wide range of wavelengths. This is further supported by model and in situ data: Figure 2a shows a wave with horizontal wavelength of $\lambda_h \geq 500$ km being excited all along Southern Andes, while the periodic temperature disturbance detected at flight level by

both GLORIA and Basic HALO Measurement and Sensor System (BAHAMAS, Krautstrunk & Giez, 2012) suggests the presence of a GW with $\lambda_h \leq 65$ km (Figure B2 in Dörnbrack et al., 2022). Recovering such a wide range of λ_h is challenging. Also, steep inclines of wavefronts in Figure 4 suggest large vertical wavelengths (λ_z), hence the full altitude range of GLORIA 3-D data from tropopause to flight altitude would be needed for the wave fitting. We therefore chose to use data from the second hexagon (due to higher flight altitude). Two S3D runs with different box sizes were performed (see Section 2.3 for details). In this section, we will analyze the results of run A, which can reliably retrieve wave parameters for waves of horizontal wavelengths 100 km $< \lambda_h <$ 900 km and vertical wavelengths of 1.2 km $< \lambda_z <$ 10.5 km. The waves with $\lambda_h <$ 100 km will be retrieved from S3D run B and considered separately is Section 3.5.

S3D wave fitting results are presented in Figure 5. Out of the total 338 (two waves were fitted for each of 169 boxes) fits, there were 76 wave fits with $\lambda_z >$ 10.5 km, these were excluded as unreliable (λ_z more than three times larger than the vertical fitting box dimension) and further 10 fits that were strong outliers in some other way (e.g., horizontal wave vector pointing in completely opposite direction to all other fits). All reliably fitted GWs naturally fall into three groups based on horizontal and vertical wavelengths (see legend of Figure 5b).

The location of the hexagonal flight pattern (right over the mountain range and extending slightly into the leeward side) clearly suggests that the observed waves are of orographic origin. Further analysis is, however, needed to confirm this. Under constant winds, orographic waves should, in theory, be stationary waves, that is, there should be no phase propagation with respect to the ground. In other words, the ground-based phase speed $\mathbf{c}_p = \omega_{gb} \mathbf{k}_h / \|\mathbf{k}_h\|^2$ should be zero. In real life conditions, winds keep changing and GWs may also interact with cloud formation processes, resulting in non-zero $\mathbf{c}_p$ (Worthington, 1999). In spite of this, $c_p = \omega_{gb}/\|\mathbf{k}_h\|$ (i.e., projection of $\mathbf{c}_p$ in the direction of $\mathbf{k}_h$) is generally lower for orographic GWs compared to other source mechanisms and typically $|c_p| <$ 10 m/s (Strube et al., 2021). As seen in Figure 5b, the wave group with $\lambda_z >$ 7 km, $\lambda_h <$ 300 km has c_p tightly distributed close to zero, and for the group with $\lambda_z <$ 7 km, $\lambda_h >$ 300 km the distribution is similarly tight, but more offset toward the negative c_p values. These results are consistent with both groups being mountain waves, but their phase lines shifting at different rates due to wind change or interaction with clouds (GLORIA observed clouds within the hexagonal flight at the altitudes of up to 8 km). The wave group with $\lambda_z >$ 7 km, $\lambda_h >$ 300 km is distributed over a wider range of c_p, but a large majority of the values are still compatible with an orographic source.

Another means of identifying GW sources from GW parameter fits is backward ray-tracing from the observation location and verifying whether waves propagate from the direction of a mountain range. Backward ray-tracing results are presented in Figure 6. It is clear that the waves with $\lambda_z >$ 7 km originate from the parts of the Andes mountain range directly below of the observation location and also mountains directly to the south of it. The backward trajectories of the waves with $\lambda_z <$ 7 km, $\lambda_h >$ 300 km extend from the Pacific coast upstream of the Andes. It is important to note that the GROGRAT ray tracer determines only whether a GW can propagate at all and therefore the source may be located at any point along the backward trajectory, and not necessarily where it begins. In this case, there are no clear source regions, other than the Andes, to which waves with such low phase speeds at these altitudes could be attributed. Also, the waves in question are long enough to be resolved in ECMWF operational analysis data. S3D wave fitting was performed on ECMWF temperatures at multiple points over the Pacific along the backward trajectories shown here and no waves similar to the ones observed by GLORIA have been identified. All wave fits over the Pacific (west of 75°W) show $|c_p| >$ 20 m/s and a very different orientation of the horizontal wave number $\mathbf{k}_h$ compared to the group of GLORIA-observed waves considered here. This indicates that the waves observed by GLORIA with $\lambda_z <$ 7 km, $\lambda_h >$ 300 km are excited over the Andes as well, but their properties are altered because of time-dependent phenomena (changing large-scale wind patterns), non-linear wave-wave interaction or cloud formation processes over the mountain chain.

3.4. Ray-Tracing and GLORIA-ALIMA Comparison

The research flight considered in this work also provided the opportunity to follow one wave packet through a large range of altitudes and compare the GLORIA GW observations to those of the ALIMA lidar higher up. To that end, the GLORIA-data based S3D wave fits discussed above were used to initialize forward ray-tracing with GROGRAT to investigate the propagation of the GLORIA-observed GWs after observation. Most of the resulting rays crossed the flight leg 5 (see Figure 2a for the location of leg 5 in the flight path) at the altitudes greater than 20 km, thus propagating through the atmospheric regions observed by ALIMA (Figure 7). This provided
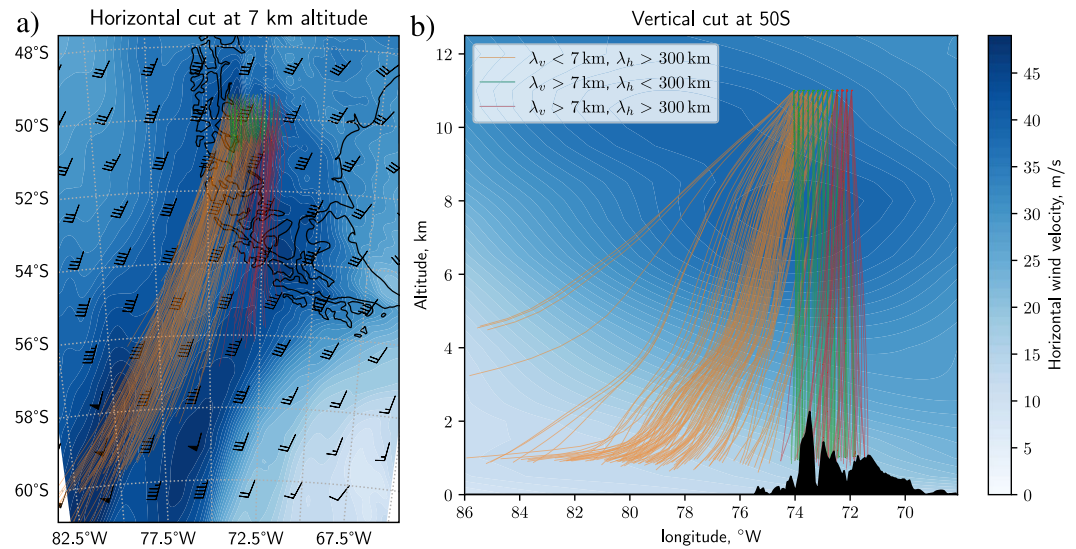
Figure 6. Backward trajectories for the waves fitted to GLORIA 3-D data. Colored lines represent rays, color shading—horizontal wind velocity. Panel (a)—horizontal map at 7 km altitude. Wind barbs as in Figure 1a. Refer to the legend and color bar of the panel (b). Panel (b)—ray projections onto a vertical cut through the atmosphere along 50°S parallel. Orography is shown in solid black.

an opportunity to compare GLORIA and ALIMA measurements by direct comparison of GW wavelengths in ALIMA data and the wavelengths and directions of GLORIA-initialized GROGRAT rays where they intersect the ALIMA observations.

The results of this comparison are presented in Figure 8. Figure 8a shows intersections of GW rays initialized from GLORIA data with the plane of ALIMA measurements from flight leg 5. The intersections are divided into four groups (c–f; marked in panel a) that are defined in terms of rectangular regions of the ALIMA curtain where the intersections take place. The corresponding spectra are then shown in panels c–f of Figure 8, respectively. The black points in the spectra indicate the wavelength values taken from the rays at the location of the intersection; the wavelength values are obtained by projecting the wave vector onto the ALIMA curtain. All intersections, except for three outlying ones, fall into these four regions.

For the comparison, it should be noted that flight leg 5 was flown just before the hexagonal flight pattern. In addition, the waves observed by GLORIA have a finite group velocity and thus took some time to reach the location of ALIMA observations. According to the ray-tracing data, the combination of both effects lead to a 5–12 hr time difference between the ALIMA observations and the most GLORIA-initialized rays reaching the same location (different rays intersect ALIMA observations at different altitudes, hence the wide time range).

Figure 8c shows the ALIMA GW spectrum from the rectangular region c depicted in Figure 8a, and the wavelengths of GLORIA rays crossing the ALIMA curtain in this area (horizontal wavelengths are projected to the plane of ALIMA observations). These rays represent GLORIA-observed waves of relatively long horizontal wavelengths (450–600 km) and short vertical wavelengths (6–7.5 km). This group demonstrates the most oblique propagation due to their relatively short vertical wavelength and wavefront orientation: the wave vectors point west, that is, around 45° from against-the-wind direction, resulting in relatively high ground-based horizontal group velocity and having long horizontal and short vertical wavelengths they have low vertical group velocity. Therefore, they cross the ALIMA curtain far inland and below 25 km altitude. There is a very good agreement between ALIMA data and wave parameters here, the rays clearly cluster at one of the two strongest ALIMA spectral peaks in the area. Note again that all rays considered in this section are initialized with $\lambda_h > 100$ km, hence the strong spectral peak around the apparent horizontal wavelength of around $\lambda_{ha} \approx 70$ km cannot be matched by GLORIA rays by design of the study. As we will see in Figure 10, waves with $\lambda_h < 100$ km initialized from GLORIA data do not get so far from the hexagon at these altitudes either. Therefore, this ALIMA peak most likely represents waves that are generated over the Andes outside the GLORIA hexagon.
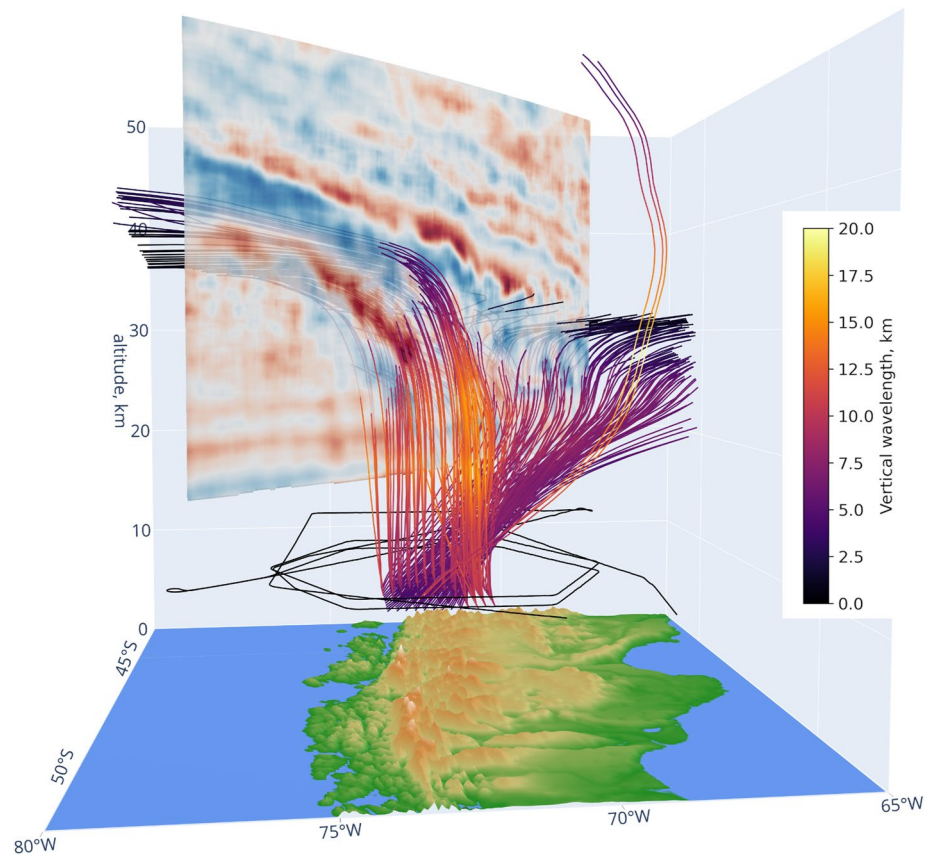
Figure 7. Rays intersecting ALIMA measurement curtain over flight leg 5. Lines with color scale represent rays, black line—flight path.

Similarly, Figure 8d shows the ALIMA GW spectrum and ray crossings from rectangle d in Figure 8a. This group of rays starts with GLORIA-observed waves of long horizontal wavelengths same as the previous group, but propagates less obliquely and crosses the ALIMA measurement curtain higher, due to wave vectors oriented more opposite to the wind (deviation from wind direction down to 25°) and longer vertical wavelength (up to 8.8 km). The vertical wavelengths of these waves decrease as they approach 35 km altitude due to decreasing horizontal winds (Figure 8b, color scale shows winds at ALIMA measurement time, black contours—when GLORIA-initialized rays start crossing ALIMA curtain). This can be seen both on ALIMA data (the second spectral peak with vertical wavelengths around 5 km becomes prominent in this region) and ray crossings. Rays that cross the curtain below about 27 km altitude do so 8–9 hr after ALIMA measurement and have wavelengths in good agreement with the ALIMA spectrum. Rays that cross higher arrive up to 18 hr after ALIMA measurement and, due to significant wind changes and a descending critical layer; have very short vertical wavelengths that do not agree with ALIMA which still measured at higher background wind conditions.

The short horizontal wavelength waves observed by GLORIA (seen as a clearly separate group in Figure 5a) cross the ALIMA curtain close to the Pacific coast, in regions e and f of Figure 8a. Due to their higher vertical wavelengths they propagate almost vertically before intersecting the ALIMA curtain and approaching the critical layer afterward. Below 26 km altitude (Figure 8e) ALIMA data shows two partially overlapping spectral peaks around horizontal wavelengths of around 200 and 120 km and data from GLORIA-initialized rays match excellently. Rays that intersect ALIMA curtain above 26 km (ray intersection region f) take up to 13hr to reach the curtain. Due to background wind changes as the waves propagate, GLORIA and ALIMA data do agree less well in Figure 8f.

One can use wavelet analysis to decompose most waves of the ALIMA data on flight leg five into two relatively coherent wave patterns (Figure 9) showing long and short waves. To that end, we chose two spectral regions in the ALIMA data, that are indicated by white rectangles of Figure 8d (longer horizontal wavelengths) and Figure 8e (shorter horizontal wavelengths), and reconstructed the waves within these spectral regions for the whole curtain.
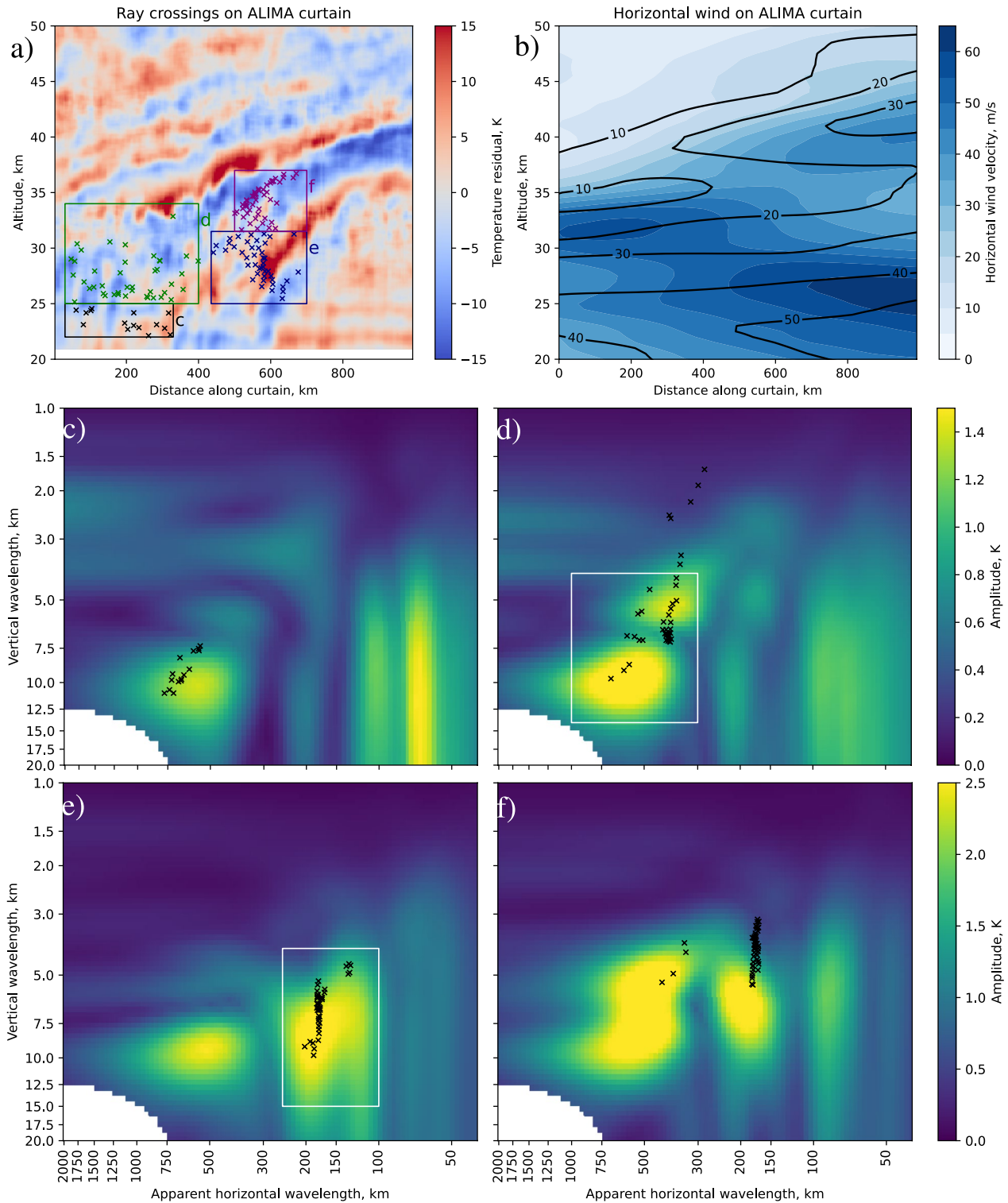
Figure 8. Comparison of ALIMA data and GW parameters obtained from GLORIA data-initialized ray-tracing. Panel (a)—ALIMA temperature residuals from flight leg 5. Distance along the curtain is measured from the start (north-western end) of the flight leg, it increases from NE to SW. Crosses indicate locations where rays cross the curtain. All intersections (except for three) were in the rectangles labeled (c–f). Panel (b)—horizontal wind velocity along the ALIMA curtain (ECMWF operational analysis). Color scale and contours show winds from 03:00 UTC and 12:00 UTC, respectively. Panels (c–f) show ALIMA GW spectra for the rectangles in panel a labeled with corresponding letters. Black crosses indicate the wave parameters of the intersecting rays (horizontal wavelengths projected to ALIMA curtain). White rectangles in panels (d and e) depict spectral regions reconstructed in Figures 9a and 9b, respectively.
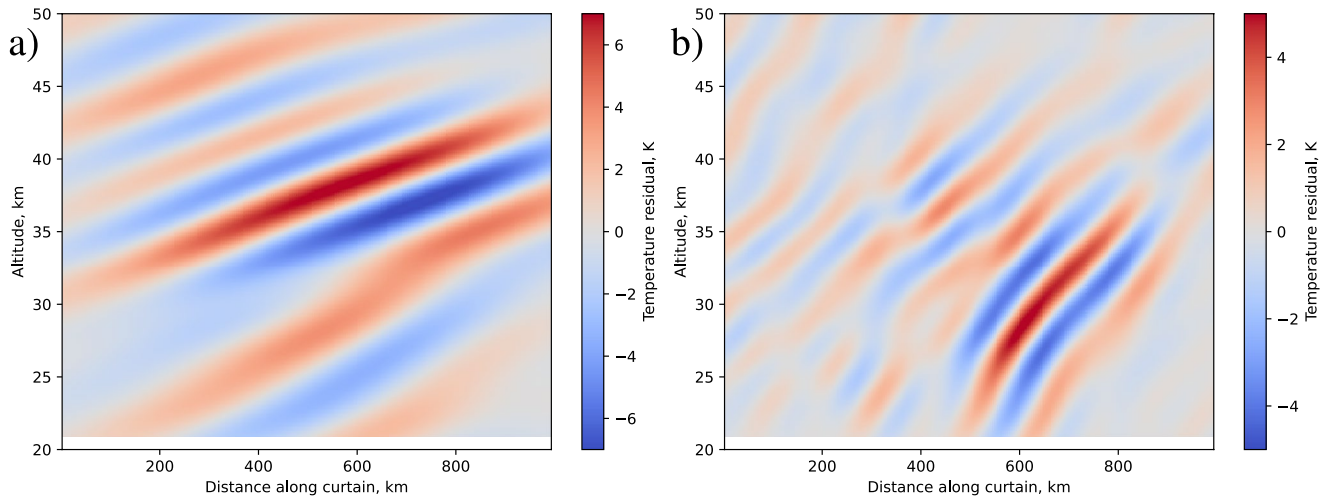
Figure 9. Panels (a and b) show temperature residuals for the flight leg 5, reconstructed from spectral regions depicted by white rectangles in Figures 8d and 8e, respectively.

Both patterns show clear evidence of vertical refraction due to vertical gradients in wind velocities and sharp decreases in wave amplitude around their critical layers. Maximal amplitudes of short waves roughly coincide with the areas where the GLORIA rays of corresponding characteristics propagate, which suggests that most of the shorter waves seen in this ALIMA curtain originate from the stretch of the Andes inside the GLORIA hexagon or close to it. However, the long wave pattern observed by ALIMA (Figure 9a) is probably excited by the whole mountain range.

In comparing GLORIA and ALIMA observations, one must remember that GLORIA only observed waves over a small portion of the Andes mountain range, and these waves propagated in various directions. Similarly, any given region of ALIMA observations can contain waves excited at different points along the mountain range, some of them previously observed by GLORIA, some not. Therefore, we formulate two conditions for GLORIA and ALIMA observations to be consistent with one another. First, GLORIA-initialized ray parameters should correspond to some peak in ALIMA spectrum at the location where they cross the region of ALIMA observations. This condition alone would already show good agreement. However, on top of it, we can formulate an additional condition that makes our claims stronger. Namely, all major peaks appearing in the ALIMA spectrum as a whole should have corresponding GLORIA-initialized rays somewhere on the ALIMA curtain, but at any given small region of ALIMA observations there might be some spectral peaks without matching GLORIA observations, in case ALIMA sees some waves excited at the Andes outside the GLORIA hexagon, and the waves from the hexagon with similar parameters simply crossed ALIMA curtain elsewhere. Based on Figure 8 and the corresponding discussion above, the first condition is met, and we believe that the second is met as well, because the most prominent structures in ALIMA spectrum are the two double peaks marked by white rectangles in the figure (which correspond to slightly different wavelengths depending on location on ALIMA curtain), and each of them have matching GLORIA-initialized rays (one peak at regions c and d, the other in the region e). We hence claim that the two instruments are in very good agreement.

3.5. Ray Tracing Short Waves

The S3D wave fitting run used to initialize all the ray-tracing introduced up to this point used fitting boxes measuring 300 km × 300 km × 3.5 km. Therefore, this run is not well suited for detecting wave packets with a horizontal extent below about 200 km and waves with $\lambda_h < 100$ km. However, such waves are seen in GLORIA temperature data in Figure 4. Also, almost all the S3D fits had wave vectors pointing in the direction between W and WSW (not shown), while GLORIA temperature structures indicate GWs with wave vectors pointing to the SW (cf. dotted magenta lines in Figures 4a and 4b). Therefore, a separate S3D run (run B, see Section 2.3) for fitting short waves was performed. In order to remove also the longer scale GWs before applying S3D, a 2D FFT high-pass filter was applied to GLORIA data to remove all waves with $\lambda_h > 150$ km. We expect to see waves with 50 km $< \lambda_h <$ 150 km, and 1.2 km $< \lambda_z <$ 10.5 km in the results of this S3D run.
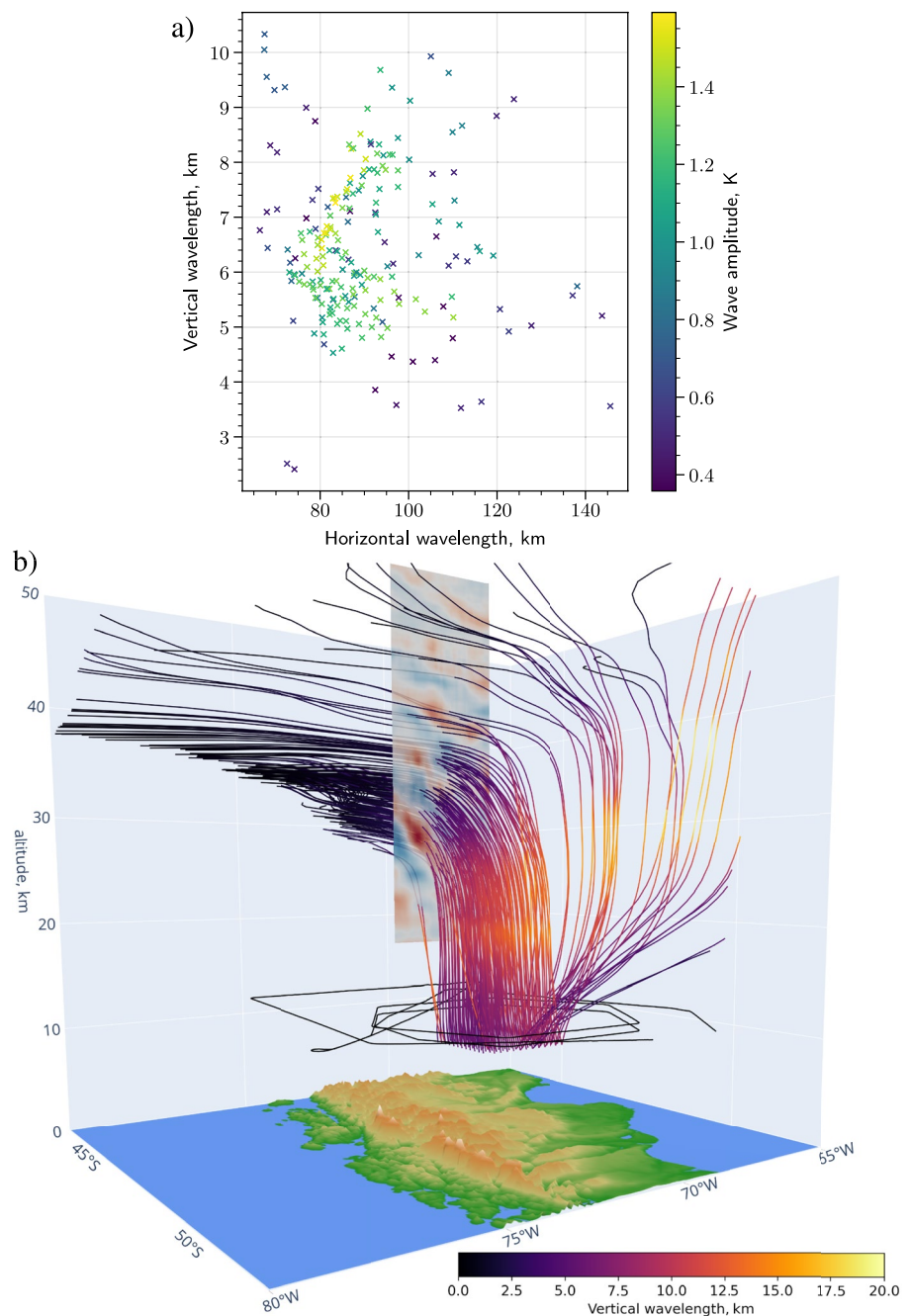
Figure 10. Panel (a)—Gravity wave parameters determined using S3D short-wave fit from measurements of the second hexagon. Color scale shows wave amplitudes. Panel (b)—GROGRAT rays initialized from short-wave S3D fit intersecting ALIMA measurement curtain over flight leg 14 (hexagon flight leg). Lines with color scale represent rays, black line—flight path.

The parameters of the fitted waves are presented in Figure 10a. A dominant horizontal wavelength of ≈80 km is found, which is in good agreement with previous findings from Alexander and Barnet (2007). The wave parameters were used to initialize the GROGRAT ray tracer and perform a comparison with ALIMA data, same as for the long-wavelength S3D fit. For comparison, ALIMA data from flight leg 14 (shown on a map in Figure 2a) was used this time, as a large number of rays cross the ALIMA curtain acquired during this leg (Figure 10b). Also, being part of the hexagonal flight pattern, leg 14 allows minimizing the time interval between ALIMA measurements and the time when GLORIA-initialized rays reach ALIMA curtain, which would have been too
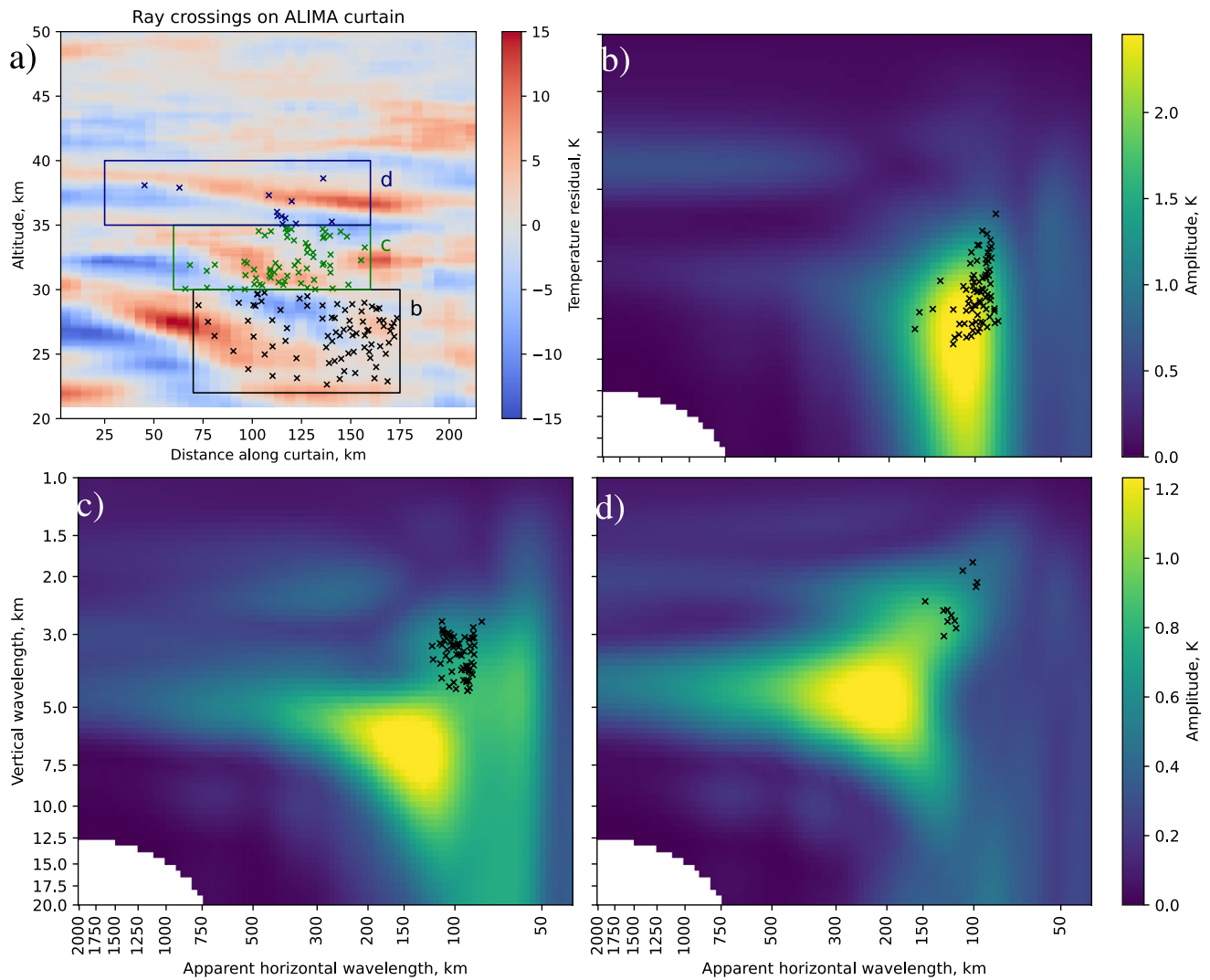
Figure 11. Similar to Figure 8, but shows GLORIA gravity wave rays crossing ALIMA observations over flight leg 14. Panel (a)—ALIMA air temperature residuals from flight leg 14. Distance along the curtain is measured from the starting point (western end) of the flight leg, hence the direction of increasing distance is W to E. Crosses indicate locations where rays cross the curtain. All intersections were located in the rectangles labeled (b–d). Panels (b–d) show ALIMA gravity wave spectra for the rectangles in panel (a) labeled with corresponding letters. Black crosses indicate the wave parameters of the intersecting rays (horizontal wavelengths projected to ALIMA curtain).

high if leg 5 was used as in Section 3.4. Finally, Figure 11 compares GLORIA and ALIMA results in the same way as it was done in Figure 8.

As one can see in Figure 10a, the high-amplitude wave fits cluster in the spectral region with $70\,\text{km} < \lambda_h < 100\,\text{km}$, and $5\,\text{km} < \lambda_z < 8\,\text{km}$. These waves follow similar trajectories to the shorter waves of the previous fit (group c in Figures 8a and 8c), initially propagating almost vertically, and then, when approaching the critical level, turning northwards or toward NW. The ALIMA spectrum below 30 km altitude (group b in Figures 11a and 11b) is dominated by short waves with the same wavelengths as GLORIA-initialized rays, demonstrating an very good match between the two instruments (note that GLORIA data is limited to $\lambda_z < 10.5\,\text{km}$, and GLORIA-initialized rays cover the majority of peak area satisfying this condition). Above 30 km altitude, the ALIMA spectrum is dominated by waves with larger λ_h (Figure 11c), but there are still some lower amplitude disturbances that match GLORIA data. Finally, there is a group of rays initialized from wave fits with initial wave vectors pointing in directions between WSW and SW (all the other fits have wave pointing between W and WSW). These waves cross the ALIMA curtain above 35 km altitude (group d in Figures 11a and 11d) having followed more complicated trajectories (Figure 10b). They match a minor peak in the ALIMA spectrum.

Most of the highest-amplitude waves analyzed in this section propagate similarly as the longer waves considered in Sections 3.3 and 3.4. Because of this, and the possible difficulties of combining results from two different S3D runs in a single analysis (waves with $\lambda_h \approx 100$ km could be double-counted and over-represented) we chose to perform all subsequent analyses using only the waves from S3D run A. Waves considered in this section (S3D run B) are, however, still important for completeness of GLORIA and ALIMA comparison.

In summary, we have validated GLORIA and ALIMA data against each other and found that all wavelengths from GROGRAT ray paths matched a major spectral peak in the ALIMA spectra, thus showing excellent agreement except where the background winds did change significantly in the time period between ALIMA measurements and the moment when the waves observed by GLORIA arrived at the same location. Also, every major peak in the ALIMA spectrum corresponds to some GLORIA-initialized rays. As GLORIA temperature structures were shown to consist of mountain waves, the major part of the wave pattern observed by ALIMA can also be explained by mountain wave activity.

3.6. GW Propagation Over the Andes

We will now use our multi-instrument observations to identify key processes that govern the most interesting aspects of the propagation of the observed GWs.

Figure 12a shows the ray traces of the shorter-λ_h wave fits (ray groups e and f in Figure 8a) together with ECMWF operational analysis data valid approximately 6 hr after observation. Waves propagate upwards quickly reaching the altitude of over 30 km in 6 hr, and then turn NW. The volume occupied by the rays agrees well with the volume where ECMWF shows strong wave activity. Most importantly, the extent of wave activity over the Pacific is very similar for both rays and ECMWF-resolved waves at all altitudes. This clearly demonstrates that waves over Pacific at around 35 km altitude that were seen in ECMWF forecasts during the campaign and suspected to be non-orographic GWs (Section 3.1) are indeed mountain waves and originate from the Andes close to the location of the hexagonal flight pattern. The longer-λ_h waves (Figure 12b; showing ray groups c and d from Figure 8a) propagate more obliquely over the South American continent (where ECMWF shows a lot of waves as well) and break upon reaching a critical layer (also as predicted by ECMWF), which is lower in that region compared to the Pacific coast.

The main features of the ray paths can be understood from linear wave theory. The GW group velocity can be expressed as (e.g., Fritts & Alexander, 2003)

$$(c_{gx}, c_{gy}, c_{gz}) = (U, V, 0) + \frac{Nm}{\sqrt{k^2 + l^2}} \frac{(km, lm, -k^2 - l^2)}{(k^2 + l^2 + m^2)^{3/2}}, \tag{7}$$

where $\mathbf{k} = (k, l, m)$ and $\mathbf{U} = (U, V)$ are wave vector and horizontal background wind vector, respectively, in Cartesian coordinates. Since typically $\lambda_h \gg \lambda_z$, $m^2 \gg l^2 + k^2$, Equation 7 implies $c_{gz} \approx N\sqrt{k^2 + l^2}/m^2$ is higher for waves with higher λ_z (lower $|m|$). This is one of the reasons why the waves of Figure 12a, with their relatively high λ_z, initially travel almost vertically and horizontal propagation only takes over near the critical layer, when λ_z decreases dramatically. The waves of Figure 12b have lower λ_z and propagate more obliquely from the start. They also reach much lower altitude during the first 6 hr of propagation, as seen in Figure 12. Quantifying the horizontal propagation distance for the whole set of observed waves is tricky due to significant variation in raypaths and the fact that waves do not break at a precisely defined location (the exact location of ray termination points depends on assumptions employed in ray tracer). Rough estimates for relatively similarly propagating wave groups can however be made. For example, the waves represented by the ray group in Figure 12a on average propagated 550 km meridionally (northward) and 540 km zonally (westwards) before breaking.

The horizontal direction of wave propagation is determined by several factors. In general, mountain waves tend to propagate along their horizontal phase lines, which mirrors the orientation of the mountain ridges (cf. e.g., Strube et al., 2021; Appendix A). This is because their ground-based horizontal phase velocity can be written as $\mathbf{c}_{gh} = \mathbf{U} + \hat{\mathbf{c}}_{gh}$, where $\hat{\mathbf{c}}_{gh}$ is the intrinsic horizontal group velocity, which is typically equal and opposite to the projection of the wind vector perpendicular to the mountain range (this results in a stationary wavefront pattern over the mountain). Therefore, the components of $\mathbf{c}_{gh}$ perpendicular to the mountain range cancel out, and $\mathbf{c}_{gh}$ is directed along the mountain range. Indeed Figure 12 shows rays initially pointing in the general northward direction, along the main Andes ridge.
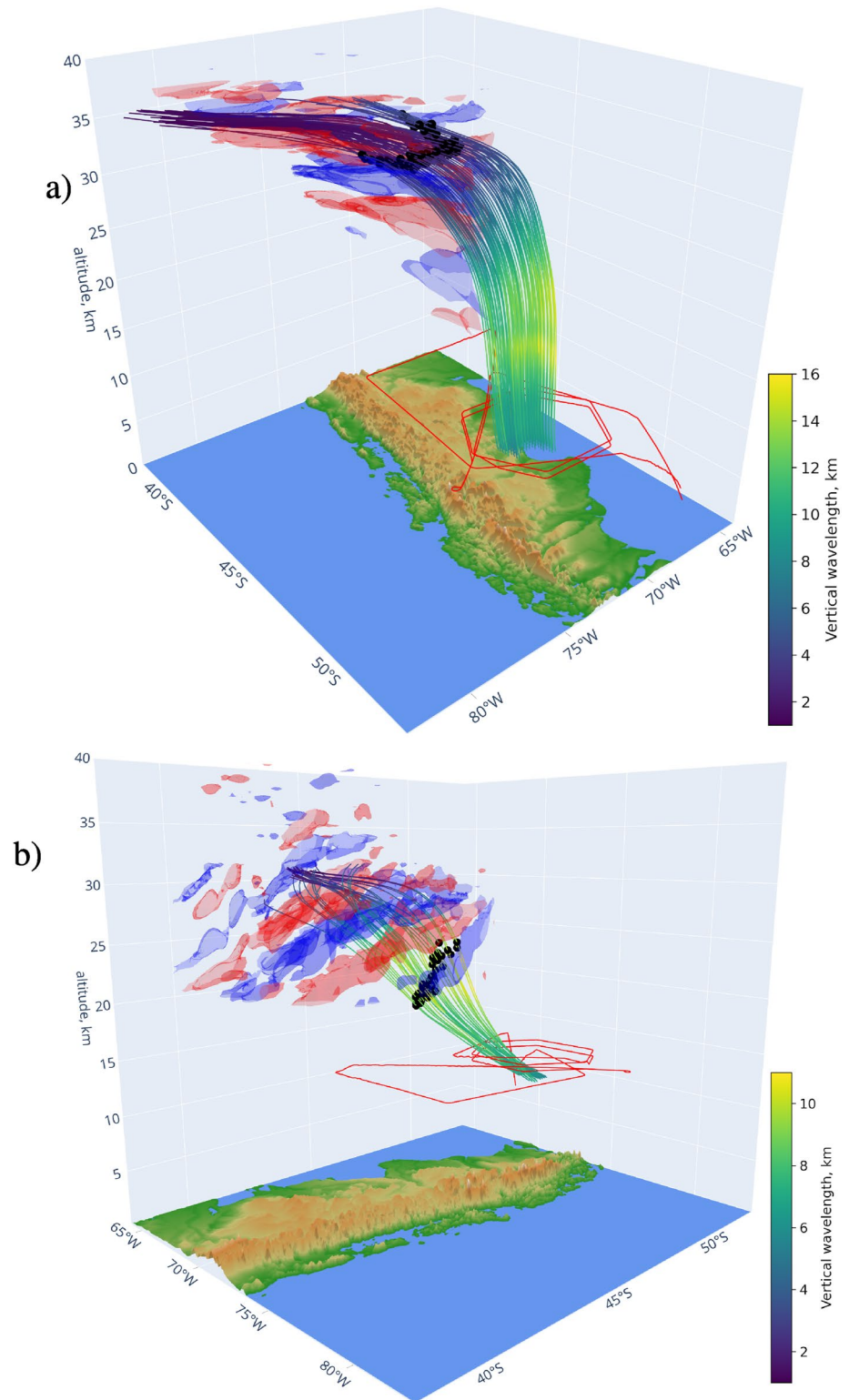
Figure 12. Rays initialized with GLORIA data (colored lines) are shown with ECMWF operational analysis temperature residuals (red and blue isosurfaces represent ±4K temperature residual, respectively) for 12:00 UTC. Black dots show wave packet positions along the ray at that time. Isosurfaces far from the rays are not shown in order not to overload the plots. Panel (a) shows short waves (ray groups e and f in Figure 8a), panel (b)—long waves (groups c and d).

The wave propagation direction can change due to horizontal refraction. Then due to horizontal wind gradients (k, l) turns (and hence $\hat{\mathbf{e}}_{gh}$, which is parallel to (k, l)). Horizontal refraction is expressed by the ray-tracing equations (e.g., Marks & Eckermann, 1995)

$$\frac{dk}{dt} \approx -k\frac{\partial U}{\partial x} - l\frac{\partial V}{\partial x} \tag{8}$$

$$\frac{dl}{dt} \approx -k\frac{\partial U}{\partial y} - l\frac{\partial V}{\partial y} \tag{9}$$

where we have omitted some small terms by neglecting the horizontal gradient of N and the latitudinal gradient of the Coriolis parameter f. In this form, the equations do not have any terms related to the zonal and meridional directions specifically and are therefore valid for any local Cartesian coordinate system on a horizontal plane. Consider a wave packet with a horizontal wave vector (k, l) and a "primed" Cartesian coordinate system (x', y') such that at with x' axis is parallel to (k, l). Then in the "primed" coordinate system $k' = \sqrt{k^2 + l^2}$, $l' = 0$, dk'/dt describes the change in horizontal wave vector magnitude, and dl''/dt describes the rotation of horizontal wave vector at the position of the wave packet. Equation 9 implies

$$\frac{dl'}{dt} = -k'\frac{\partial U'}{\partial y'}, \tag{10}$$

that is, horizontal refraction occurs, if the wind component parallel to the wave vector has a gradient perpendicular to the wave vector. The angular velocity of rotation is

$$\frac{d\alpha}{dt} = \frac{1}{k'}\frac{dl'}{dt} = -\frac{\partial U'}{\partial y'} = -\frac{(-l, k)}{\sqrt{l^2 + k^2}} \cdot \nabla\left(\frac{(U, V) \cdot (k, l)}{\sqrt{l^2 + k^2}}\right) = \frac{l^2 V_x - k^2 U_y + lk(U_x - V_y)}{l^2 + k^2}, \tag{11}$$

where $U_x = \partial U/\partial x$, etc.

The horizontal wind gradients that cause the refraction of the waves in our study are visible in Figure 13a, which presents the zonal and meridional winds on a vertical section going north from the center of the hexagonal flight pattern. Figure 13b shows the evolution of wave vector azimuth for the GLORIA-initialized GROGRAT rays as they propagated upwards. Very strong horizontal refraction is evident, with some rays turning by as much as 70°. This also explains why the waves over the Pacific had unexpected orientation (e.g., Figure 2b), causing speculation of non-orographic waves during flight planning. The ray-tracing predictions are confirmed by the ALIMA observations, as wrong wave orientation would inevitably result in wrong wavelengths on the ALIMA plane of observation. We took one strongly refracted ray (Figure 13c) as an example to demonstrate that our simplified framework to explain horizontal refraction with horizontal wind gradients (Equations 8–11) accounts for the majority of wind vector rotation predicted by the ray tracer. The agreement between the two methods becomes worse close to the critical level, as the terms neglected in Equations 8 and 9 are no longer small when the wave attains very low group velocities.

Refraction of such strength is significant, as GWs carry horizontal momentum that is parallel to the wave vector. Turning of the vector implies momentum exchange between the waves and the background wind field, which can have a significant impact on the winds (e.g., Buehler & McIntyre, 2003). The study presented in this paper is local by nature. GLORIA observations only cover a relatively small stretch of the Andes, and GWs observed by ALIMA at higher altitudes are clearly excited by GWs originating from mountains to the east of the Andes main ridge as well. Therefore, we cannot quantify the impact on the background flow just using the data presented here, but we can show that horizontal refraction plays a crucial role on whatever impact mountains waves can have on middle atmosphere dynamics.

Zonal and meridional GWMF for the GROGRAT rays used in this study is presented in Figure 14. One can see that horizontal refraction significantly alters GWMF. There are some waves that are excited with negligible meridional GWMF, refract significantly while propagating from 15 to 26 km altitude and hence acquire a meridional GWMF value of the same order as their initial zonal GWMF, and deposit this momentum in the altitudes from 25 to 30 km reaching their critical level. In particular, the vector of total GWMF carried by all the traced waves rotates by 18° as waves propagate from 11 km altitude to 26 km altitude, just before some waves begin to brake. The ratio of meridional GWMF and total GWMF $F_{py}/\sqrt{F_{px}^2 + F_{py}^2}$ increases from 0.18 at 11 km altitude to 0.46 at 26 km altitude. This clearly shows that horizontal refraction must be considered when studying the
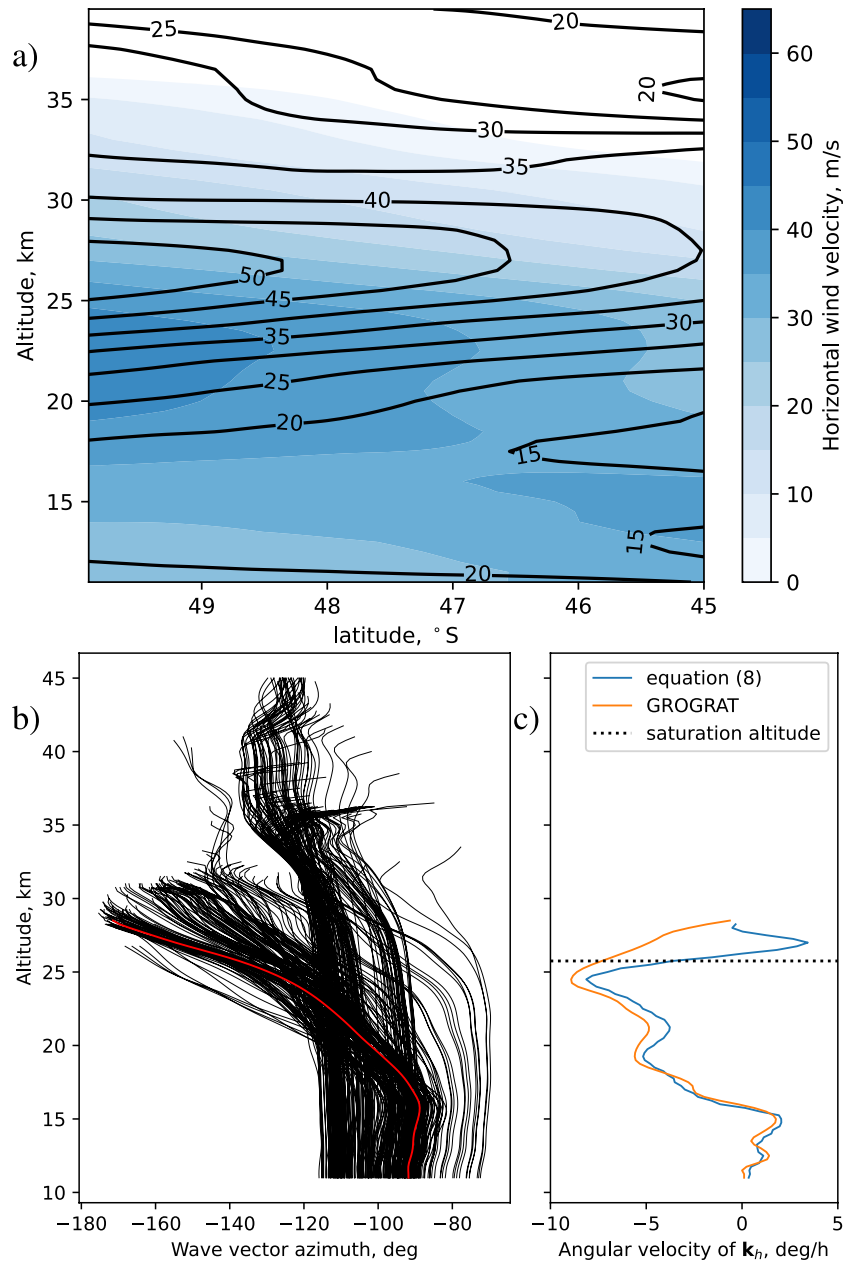
Figure 13. Panel (a)—horizontal winds on a vertical section through the center of the hexagonal flight pattern oriented in meridional direction. Color scale—zonal wind, contours—meridional wind. Panel (b)—direction of the wave vector, positive values clockwise from due N. Panel (c)—angular velocity of the horizontal wave vector for the ray highlighted in red in the panel (b), left. Orange line—as calculated by the ray tracer, blue line—simple estimate based on Equation 11. Black dots mark the altitude where the ray reached saturation (just below critical level).

effects of GWs on the middle atmosphere circulation. Though effects of such wave direction changes were studied theoretically (Buehler & McIntyre, 2003) and in using models (Preusse et al., 2009), only the SouthTRAC campaign allowed to observe and quantify this effect in nature for the first time. The ECMWF-resolved waves further support these findings.
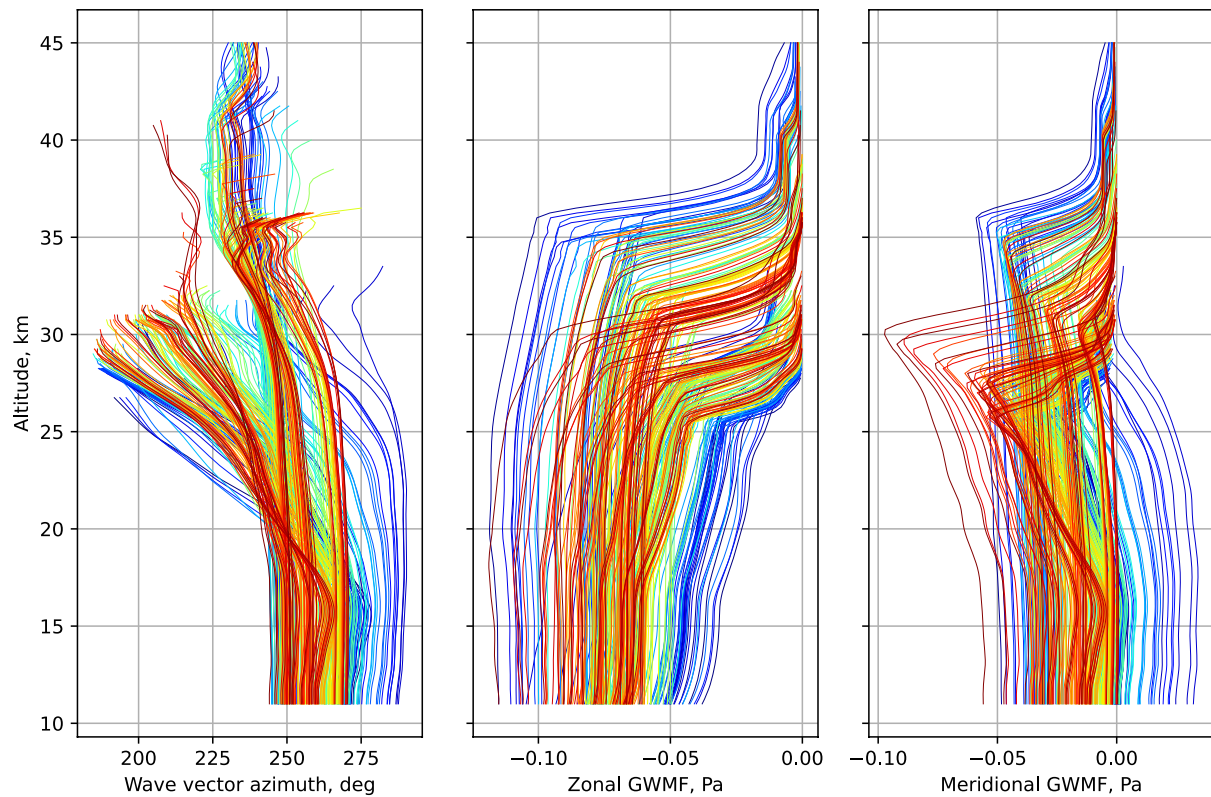
Figure 14. The evolution of wave vector azimuth and both components of the horizontal gravity wave momentum flux (GWMF) with altitude for each GROGRAT ray in our study. The different colors of the lines were only used to improve readability of the figure, they carry no special meaning.

3.7. MWM Results and Model Comparison

The MWM (see Section 2.5) is tested by modeling GWs observed during the measurement flight analyzed in this paper and comparing the results to GLORIA and ALIMA data. Figure 15 compares actual GLORIA measurement to MWM simulation results with GLORIA observational filter applied. The observational filter is realized by generating synthetic GLORIA observations from MWM temperature data with the GLORIA radiance forward model and applying the same tomographic retrieval as for the real observations. One can see that the MWM captured the major features of the waves inside the hexagon, such as a high-amplitude wave almost parallel to the mountain ridges around the center of the hexagon and short waves in its eastern half. However, there are significant differences as well: MWM data has a strong positive temperature anomaly in the north of the hexagon which is not seen in the actual GLORIA data. Also, MWM data shows a group of waves with east-west wavefront orientation on the eastern side of the hexagon that GLORIA did not observe. Within the MWM, these waves were excited over mountain ridges of east-west orientation deep inland in South America. It is possible that the actual wind over these ridges was weaker than the model expected due to blocking or complex wind interaction with the main part of the Andes.

Figure 16 shows a comparison of ALIMA observations from three flight legs with significant GW activity to MWM and ECMWF data. MWM seems to predict the strongest wave activity in correct locations, but the dominant wavelengths in MWM seem to be systematically shorter than seen in ALIMA data. It is possible that the longer waves, which are excited by wind interaction with large scale features (such as the whole mountain range) are not adequately represented in MWM. ECMWF data only has sufficient resolution to capture the longest waves in the ALIMA spectrum. These are represented well in most locations, but there are still some puzzling discrepancies, such as an almost complete lack of waves over the Pacific below around 35 km altitude (leg 3 and leg 5 after the 700 km mark). Also, even the highest amplitude, long wave that dominated flight leg 5 only has a low-amplitude extension over the Pacific. For these problematic areas, waves seem to be missing in MWM data as well. Observations are clearly still needed to improve model performance for mountain waves.
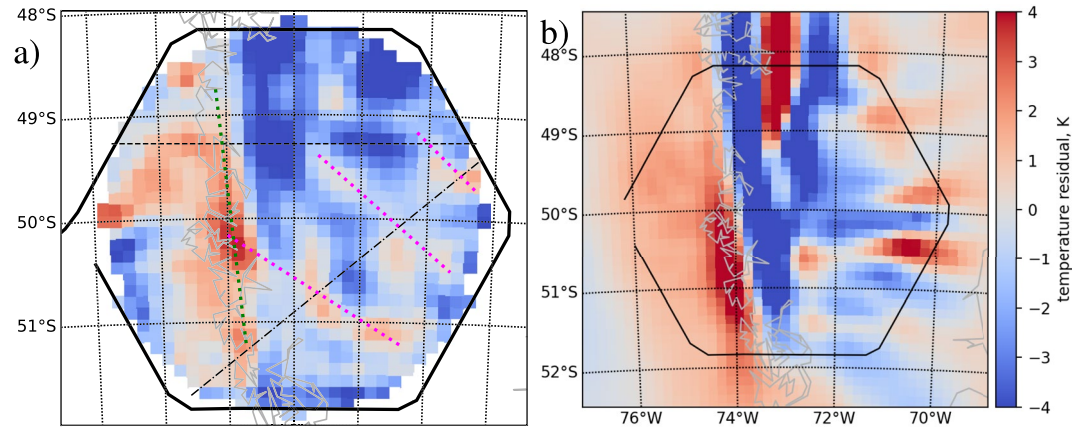
Figure 15. Panels show a horizontal cut at 12 km altitude through the GLORIA 3D tomography volume. Panel (a) shows actual GLORIA data retrieved from the second hexagon (repeated from Figure 4), panel (b) mountain wave model data with GLORIA observational filter.
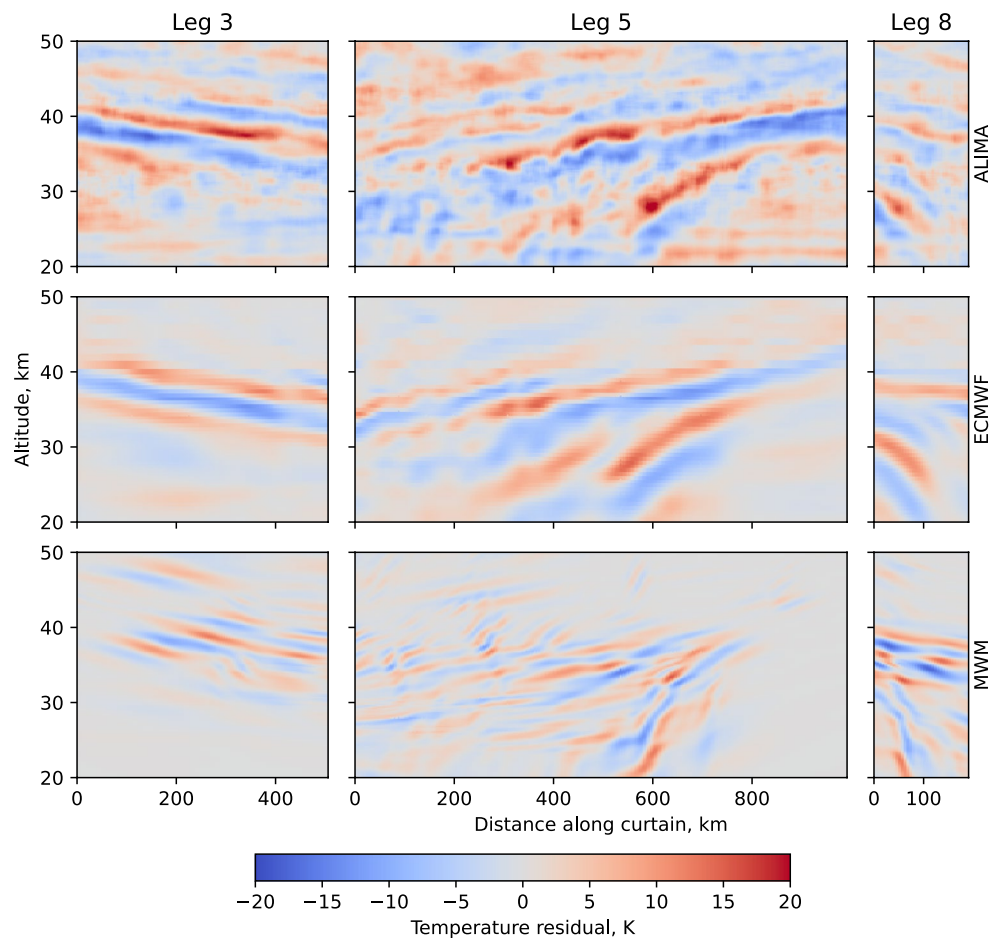

Figure 16. A comparison between ALIMA data, ECMWF operational analysis, and MWM simulations for flight legs 3, 5, and 8. Positions of each leg can be seen on the map in Figure 2a, marked L3, L5, L8, respectively.

4. Conclusions

The SouthTRAC aircraft measurement campaign was carried out in September–November 2019 with the German HALO research aircraft. Here we present the measurements by the GLORIA infrared limb imager and by the ALIMA lidar from a measurement flight on 20–21 September that observed a high amplitude mountain wave pattern over the Andes.

This flight included a hexagonal flight pattern around part of the Andes and the Pacific coast, which allowed us to perform a 3-D tomographic temperature retrieval within the hexagonal flight pattern at the altitude range from 8 to 13 km. GLORIA is the only instrument capable to retrieve 3-D data of such detail in the UTLS region. The data revealed a complex GW pattern that included a wide variety of wavelengths and different wavefront orientations. GW amplitudes and their full 3-D wave vectors were obtained from the GLORIA observations using small-volume least squares fitting of sinusoidal plane waves. Since, according to linear theory, amplitudes and wave vectors fully describe a GW, we were able to use GLORIA data to initialize the GROGRAT ray tracer. Ray-tracing results confirmed that the observed waves were excited over the Andes and propagated obliquely. The ray-tracer also allows us to predict wave propagation after the measurement. Most of these GLORIA-initialized rays propagated through the atmospheric regions observed by the ALIMA lidar, allowing us to compare the data sets provided by the two instruments. Very good agreement was found: the wavelengths of GLORIA rays, as they were crossing the volumes with ALIMA observations, matched the spectral peaks of ALIMA data everywhere except for the cases with very long ray travel times (i.e., when the GLORIA-initialized rays arrived at the location of the ALIMA observations more than about 12 hr after the measurement). Also, every major peak in the ALIMA spectrum had corresponding GLORIA-initialized rays. These rays could be back-traced to orography, which strongly suggests that the wave pattern observed by both GLORIA and ALIMA could be explained by mountain wave activity, at least to a large extent. These results serve as a validation for our least squares wave-fitting technique (S3D) and ray-tracing code (GROGRAT).

Rays initialized from GLORIA data generally occupied the same volumes where ECMWF operational analyses showed enhanced wave activity. There was one wave pattern in ECMWF data (present both in operational analysis and in forecast data available before the flight) that was of particular interest: at altitudes of around 30 km wave activity was strong over the ocean west of the Andes main ridge and thus seemingly upstream of the Andes. These GWs did not appear to be of orographic origin due to their position and wavefront orientation. We showed, based on both GLORIA and ALIMA data, which these waves did indeed originate from the Andes, but had been excited south of their observed location, had experienced strong horizontal refraction and propagated along their phase fronts toward the west of the main ridge. The ECMWF-IFS in its configuration of 2019 resolves waves with wavelength longer than 100 km. Compared to ALIMA observations, the ECMWF data captured most of these meso-scale waves well, but there are some notable differences between model and observations. For example, ECMWF had significantly lower GW amplitudes in the part of the wave pattern that extended over the Pacific. The same difference was found for the MWM, which also underestimated this part of the wavefield. A possible reason for this discrepancy in MWM would be inaccurate representation of excitation of mountain waves with long horizontal wavelengths, as these generally tend to propagate furthest in the horizontal direction. The main features of GLORIA and ALIMA observations were predicted by the MWM, but the model tended to underestimate vertical wavelengths in the stratosphere and overestimate the amplitudes of waves excited by wind flow over minor ridges.

The combination of GLORIA and ALIMA data allowed to directly observe horizontal refraction by comparing the horizontal wavelengths of the GLORIA-initialized rays and the horizontal wavelengths from ALIMA, which to our knowledge has not been performed before and is a unique success of the coincident observational techniques employed in the SouthTRAC campaign. In our case study, horizontal refraction played a major part in shaping the overall wave structure and the interaction with the background flow. Most of the waves were excited with wavefronts parallel to the main mountain ridge as confirmed by the GLORIA observations. At larger altitudes, however, the waves had turned by about 45° and wave vectors pointed to the south-west. Due to this turn of the wave vector, and the nature of the wind profile, the bulk of the waves moved from the center of the hexagon to the North and East, that is, the ground-based wave group velocity was oriented meridionally rather than zonally, which amounts to significant meridional transport of zonal momentum. The inability if current GCMs to adequately represent this process contributes to the problem of the missing GW drag at 60°S. Also, most of the observed waves carried almost no meridional momentum at the time they were excited at the Andes, but

some acquired so much meridional momentum due to horizontal refraction, that they deposited more meridional than zonal momentum at the critical layer. This demonstrates that current parametrizations with only vertical propagation and no refraction neglect important features of the wave driving both in terms of location and direction of the exerted drag. Therefore, the effect such waves have on the general circulation cannot be adequately represented without more detailed representations of GWs in general circulation models. Further development of the models should be constrained by high-resolution observations. Our results also suggest that, at least in the presence of horizontal wind shear, significant momentum exchange between GWs and the background flow can occur without wave breaking, which is often overlooked while identifying regions where GW drag can occur. The current case can provide such a ground truth, but global data would be required to quantify the effect on the global circulation. Observations similar to the ones presented here could be performed for all regions of the Earth and on a regular basis by bringing an infrared limb sounder into space. GLORIA demonstrates that the technique is mature and provides data of high quality.

Data Availability Statement

GLORIA and ALIMA data from the SouthTRAC campaign flight presented here are openly accessible via the Zenodo database (Krasauskas et al., 2022) operated by CERN (Conseil Européen pour la Recherche Nucléaire). ECMWF operational analysis data is available from ECMWF https://www.ecmwf.int/en/forecasts/datasets.

References

Alexander, M. J., & Barnet, C. D. (2007). Using satellite observations to constrain gravity wave parameterizations for global models. *Journal of the Atmospheric Sciences*, *64*(5), 1652–1665. https://doi.org/10.1175/jas3897.1

Alexander, M. J., & Dunkerton, T. J. (1999). A spectral parameterization of mean-flow forcing due to breaking gravity waves. *Journal of the Atmospheric Sciences*, *56*(24), 4167–4182. https://doi.org/10.1175/1520-0469(1999)056<4167:aspomf>2.0.co;2

Alexander, M. J., & Rosenlof, K. H. (2003). Gravity-wave forcing in the stratosphere: Observational constraints from the upper atmosphere research satellite and implications for parameterization in global models. *Journal of Geophysical Research*, *108*(D19), 4597. https://doi.org/10.1029/2003JD003373

Amante, C., & Eakins, B. (2009). *Etopo1 1 arc-minute global relief model: Procedures, data sources, and analysis*. National Centers for Environmental Information, NESDIS, NOAA, U.S. Department of Commerce. (Last access: 20 February 2020). https://doi.org/10.7289/V5C8276M

Andrews, D. G., Holton, J. R., & Leovy, C. B. (1987). *Middle atmosphere dynamics* (Vol. 40). Academic Press.

Bacmeister, J. T. (1993). Mountain-wave drag in the stratosphere and mesosphere inferred from observed winds and a simple mountain-wave parameterization scheme. *Journal of the Atmospheric Sciences*, *50*(3), 377–399. https://doi.org/10.1175/1520-0469(1993)050<0377:mwdits>2.0.co;2

Bacmeister, J. T., Newman, P., Gary, B., & Chan, K. (1994). An algorithm for forecasting mountain wave-related turbulence in the stratosphere. *Weather and Forecasting*, *9*(2), 241–253. https://doi.org/10.1175/1520-0434(1994)009<0241:AAFFMW>2.0.CO;2

Becker, E., & Vadas, S. L. (2018). Secondary gravity waves in the winter mesosphere: Results from a high-resolution global circulation model. *Journal of Geophysical Research: Atmospheres*, *123*(5), 2605–2627. https://doi.org/10.1002/2017JD027460

Buehler, O., & McIntyre, M. E. (2003). Remote recoil: A new wave-mean interaction effect. *Journal of Fluid Mechanics*, *492*, 207–230. https://doi.org/10.1017/s0022112003005639

Bühler, O., McIntyre, M. E., & Scinocca, J. F. (1999). On shear-generated gravity waves that reach the mesosphere. Part I: Wave generation. *Journal of the Atmospheric Sciences*, *56*(21), 3749–3773. https://doi.org/10.1175/1520-0469(1999)056<3749:osggwt>2.0.co;2

Butchart, N., Charlton-Perez, A. J., Cionni, I., Hardiman, S. C., Haynes, P. H., Krueger, K., et al. (2011). Multimodel climate and variability of the stratosphere. *Journal of Geophysical Research*, *116*(D5), D05102. https://doi.org/10.1029/2010JD014995

Cao, B., Heale, C. J., Guo, Y., Liu, A. Z., & Snively, J. B. (2016). Observation and modeling of gravity wave propagation through reflection and critical layers above Andes lidar observatory at Cerro Pachón, Chile. *Journal of Geophysical Research: Atmospheres*, *121*(21), 12737–12750. https://doi.org/10.1002/2016JD025173

Charron, M., & Manzini, E. (2002). Gravity waves from fronts: Parameterization and middle atmosphere response in a general circulation model. *Journal of the Atmospheric Sciences*, *59*(5), 923–941. https://doi.org/10.1175/1520-0469(2002)059<0923:gwffpa>2.0.co;2

Chen, C.-C., Durran, D. R., & Hakim, G. J. (2005). Mountain-wave momentum flux in an evolving synoptic-scale flow. *Journal of the Atmospheric Sciences*, *62*(9), 3213–3231. https://doi.org/10.1175/JAS3543.1

Choi, H.-J., Chun, H.-Y., & Song, I.-S. (2009). Gravity wave temperature variance calculated using the ray-based spectral parameterization of convective gravity waves and its comparison with Microwave Limb Sounder observations. *Journal of Geophysical Research*, *114*(D8), D08111. https://doi.org/10.1029/2008JD011330

Copernicus Climate Change Service (C3S). (2017). Era5: Fifth generation of ECMWF atmospheric reanalyses of the global climate. Copernicus Climate Change Service Climate Data Store (CDS). Retrieved from https://cds.climate.copernicus.eu/cdsapp#!/home

Curtis, A. R. (1952). Discussion of "A statistical model for water vapor absorption" by R. M. Goody. *Quarterly Journal of the Royal Meteorological Society*, *78*, 638–640.

Dee, D. P., Uppala, S. M., Simmons, A. J., Berrisford, P., Poli, P., Kobayashi, S., et al. (2011). The ERA-Interim reanalysis: Configuration and performance of the data assimilation system. *Quarterly Journal of the Royal Meteorological Society*, *137*(656), 553–597. https://doi.org/10.1002/qj.828

de Groot-Hedlin, C. D., Hedlin, M. A. H., Hoffmann, L., Alexander, M. J., & Stephan, C. C. (2017). Relationships between gravity waves observed at Earth's surface and in the stratosphere over the central and eastern United States. *Journal of Geophysical Research: Atmospheres*, *122*(21), 11482–11498. https://doi.org/10.1002/2017JD027159

dela Camara, A., Lott, F., & Hertzog, A. (2014). Intermittency in a stochastic parameterization of nonorographic gravity waves. *Journal of Geophysical Research: Atmospheres*, *119*(21), 11905–11919. https://doi.org/10.1002/2014JD022002

dela Torre, A., Hierro, R., Llamedo, P., & Alexander, P. (2011). Severe hailstorms near Southern Andes in the presence of mountain waves. *Atmospheric Research*, *101*(1–2), 112–123. https://doi.org/10.1016/j.atmosres.2011.01.015

Dörnbrack, A., Bechtold, P., & Schumann, U. (2022). High-resolution aircraft observations of turbulence and waves in the free atmosphere and comparison with global model predictions. *Journal of Geophysical Research: Atmospheres*, *127*(16), e2022JD036654. https://doi.org/10.1029/2022JD036654

Dunkerton, T. J. (1997). Shear instability of internal inertia-gravity waves. *Journal of the Atmospheric Sciences*, *54*(12), 1628–1641. https://doi.org/10.1175/1520-0469(1997)054<1628:sioiig>2.0.co;2

Eckermann, S. D., & Preusse, P. (1999). Global measurements of stratospheric mountain waves from space. *Science*, *286*(5444), 1534–1537. https://doi.org/10.1126/science.286.5444.1534

Einaudi, F., & Hines, C. O. (1970). WKB approximation in application to acoustic-gravity waves. *Canadian Journal of Physics*, *48*(12), 1458–1471. https://doi.org/10.1139/p70-185

Ern, M., Hoffmann, L., & Preusse, P. (2017). Directional gravity wave momentum fluxes in the stratosphere derived from high-resolution AIRS temperature data. *Geophysical Research Letters*, *44*(1), 475–485. https://doi.org/10.1002/2016GL072007

Ern, M., Hoffmann, L., Rhode, S., & Preusse, P. (2022). The mesoscale gravity wave response to the 2022 Tonga volcanic eruption: AIRS and MLS satellite observations and source backtracing. *Geophysical Research Letters*, *49*(10). https://doi.org/10.1029/2022GL098626

Ern, M., Ploeger, F., Preusse, P., Gille, J. C., Gray, L. J., Kalisch, S., et al. (2014). Interaction of gravity waves with the QBO: A satellite perspective. *Journal of Geophysical Research: Atmospheres*, *119*(5), 2329–2355. https://doi.org/10.1002/2013JD020731

Ern, M., Preusse, P., & Riese, M. (2015). Driving of the SAO by gravity waves as observed from satellite. *Annales Geophysicae*, *33*(4), 483–504. https://doi.org/10.5194/angeo-33-483-2015

Ern, M., Preusse, P., & Warner, C. D. (2006). Some experimental constraints for spectral parameters used in the Warner and McIntyre gravity wave parameterization scheme. *Atmospheric Chemistry and Physics*, *6*(12), 4361–4381. https://doi.org/10.5194/acp-6-4361-2006

Ern, M., Trinh, Q. T., Kaufmann, M., Krisch, I., Preusse, P., Ungermann, J., et al. (2016). Satellite observations of middle atmosphere gravity wave absolute momentum flux and of its vertical gradient during recent stratospheric warmings. *Atmospheric Chemistry and Physics*, *16*(15), 9983–10019. https://doi.org/10.5194/acp-16-9983-2016

Ern, M., Trinh, Q. T., Preusse, P., Gille, J. C., Mlynczak, M. G., Russell, J. M., III, & Riese, M. (2018). GRACILE: A comprehensive climatology of atmospheric gravity wave parameters based on satellite limb soundings. *Earth System Science Data*, *10*(2), 857–892. https://doi.org/10.5194/essd-10-857-2018

Fovell, R., Durran, D., & Holton, J. R. (1992). Numerical simulations of convectively generated stratospheric gravity waves. *Journal of the Atmospheric Sciences*, *49*(16), 1427–1442. https://doi.org/10.1175/1520-0469(1992)049<1427:nsocgs>2.0.co;2

Friedl-Vallon, F., Gulde, T., Hase, F., Kleinert, A., Kulessa, T., Maucher, G., et al. (2014). Instrument concept of the imaging Fourier transform spectrometer GLORIA. *Atmospheric Measurement Techniques*, *7*(10), 3565–3577. https://doi.org/10.5194/amt-7-3565-2014

Fritts, D., & Alexander, M. (2003). Gravity wave dynamics and effects in the middle atmosphere. *Reviews of Geophysics*, *41*(1). https://doi.org/10.1029/2001RG000106

Garcia, R. R., Marsh, D., Kinnison, D. E., Boville, B., & Sassi, F. (2007). Simulations of secular trends in the middle atmosphere 1950–2003. *Journal of Geophysical Research*, *112*(D9), D09301. https://doi.org/10.1029/2006JD007485

Garcia, R. R., Smith, A. K., Kinnison, D. E., dela Camara, A., & Murphy, D. J. (2017). Modification of the gravity wave parameterization in the whole atmosphere community climate model: Motivation and results. *Journal of the Atmospheric Sciences*, *74*(1), 275–291. https://doi.org/10.1175/JAS-D-16-0104.1

Garcia, R. R., & Solomon, S. (1985). The effect of breaking gravity waves on the dynamics and chemical composition of the mesosphere and lower thermosphere. *Journal of Geophysical Research*, *90*(D2), 3850–3868. https://doi.org/10.1029/jd090id02p03850

Geldenhuys, M., Kaifler, B., Preusse, P., Ungermann, J., Alexander, P., Krasauskas, L., et al. (2022). Observations of gravity wave refraction and its causes and consequences. *Journal of Geophysical Research: Atmospheres*. https://doi.org/10.1002/essoar.10511036.1

Geldenhuys, M., Preusse, P., Krisch, I., Zülicke, C., Ungermann, J., Ern, M., & Riese, M. (2021). Orographically induced spontaneous imbalance within the jet causing a large-scale gravity wave event. *Atmospheric Chemistry and Physics*, *21*(13), 10393–10412. https://doi.org/10.5194/acp-21-10393-2021

Gille, J. C., Barnett, J. J., Whitney, J. G., Dials, M. A., Woodard, D., Rudolf, W. P., & Mankin, W. (2003). The High-Resolution Dynamics Limb Sounder (HIRDLS) experiment on AURA. *Proceedings of SPIE*, *5152*, 161–171. https://doi.org/10.1117/12.507657

Godson, W. L. (1953). The evaluation of infra-red radiative fluxes due to atmospheric water vapor. *Quarterly Journal of the Royal Meteorological Society*, *79*(341), 367–379. https://doi.org/10.1002/qj.49707934104

Gordley, L. L., & Russell, J. M. (1981). Rapid inversion of limb radiance data using an emissivity growth approximation. *Applied Optics*, *20*(5), 807–813. https://doi.org/10.1364/AO.20.000807

Hasha, A., Bühler, O., & Scinocca, J. (2008). Gravity wave refraction by three-dimensionally varying winds and the global transport of angular momentum. *Journal of the Atmospheric Sciences*, *65*(9), 2892–2906. https://doi.org/10.1175/2007jas2561.1

Hersbach, H., Bell, B., Berrisford, P., Biavati, G., Horányi, A., Muñoz Sabater, J., & Thpaut, J.-N. (2018). ERA5 hourly data on pressure levels from 1979 to the present. *Copernicus Climate Change Service (C3S) Climate Data Store (CDS)*. https://doi.org/10.24381/cds.bd0915c6

Hertzog, A., Boccara, G., Vincent, R. A., Vial, F., & Cocquerez, P. (2008). Estimation of gravity wave momentum flux and phase speeds from quasi-Lagrangian stratospheric balloon flights. Part II: Results from the Vorcore campaign in Antarctica. *Journal of the Atmospheric Sciences*, *65*(10), 3056–3070. https://doi.org/10.1175/2008JAS2710.1

Hestenes, M. R., & Stiefel, E. (1952). Methods of conjugate gradients for solving linear systems. *Journal of Research of the NIST*, *49*(6), 409–436. https://doi.org/10.6028/jres.049.044

Hindley, N. P., Wright, C. J., Hoffmann, L., Moffat-Griffin, T., & Mitchell, N. J. (2020). An 18 yr climatology of directional stratospheric gravity wave momentum flux from 3-D satellite observations. *Geophysical Research Letters*, *47*(22), e2020GL089557. https://doi.org/10.1029/2020GL089557

Hindley, N. P., Wright, C. J., Smith, N. D., Hoffmann, L., Holt, L. A., Alexander, M. J., & Mitchell, N. J. (2019). Gravity waves in the winter stratosphere over the southern ocean: High-resolution satellite observations and 3-D spectral analysis. *Atmospheric Chemistry and Physics*, *19*(24), 15377–15414. https://doi.org/10.5194/acp-19-15377-2019

Hindley, N. P., Wright, C. J., Smith, N. D., & Mitchell, N. J. (2015). The southern stratospheric gravity wave hot spot: Individual waves and their momentum fluxes measured by COSMIC GPS-RO. *Atmospheric Chemistry and Physics*, *15*(14), 7797–7818. https://doi.org/10.5194/acp-15-7797-2015

Hoffmann, L., & Alexander, M. J. (2009). Retrieval of stratospheric temperatures from Atmospheric Infrared Sounder radiance measurements for gravity wave studies. *Journal of Geophysical Research*, *114*(D7), D07105. https://doi.org/10.1029/2008JD011241

Hoffmann, L., Grimsdell, A. W., & Alexander, M. J. (2016). Stratospheric gravity waves at Southern Hemisphere orographic hotspots: 2003–2014 AIRS/AQUA observations. *Atmospheric Chemistry and Physics*, *16*(14), 9381–9397. https://doi.org/10.5194/acp-16-9381-2016

Hoffmann, L., Kaufmann, M., Spang, R., Müller, R., Remedios, J. J., Moore, D. P., & Riese, M. (2008). Envisat MIPAS measurements of CFC-11: Retrieval, validation, and climatology. *Atmospheric Chemistry and Physics*, *8*(5), 3671–3688. https://doi.org/10.1016/j.asr.2005.03.112

Holton, J. R. (2004). *An introduction to dynamic meteorology* (3rd ed.). Academic Press Limited.

Holton, J. R., & Alexander, M. J. (2000). *The role of waves in the transport circulation of the middle atmosphere* (Vol. 123). American Geophysical Union.

Jiang, J., Wang, B., Goya, K., Hocke, K., Eckermann, S., Ma, J., & Read, W. (2004). Geographical distribution and interseasonal variability of tropical deep convection: UARS MLS observations and analyses. *Journal of Geophysical Research*, *109*(D3). https://doi.org/10.1029/2003JD003756

Kaifler, B., & Kaifler, N. (2021). A compact Rayleigh autonomous lidar (coral) for the middle atmosphere. *Atmospheric Measurement Techniques*, *14*(2), 1715–1732. https://doi.org/10.5194/amt-14-1715-2021

Kalisch, S., Preusse, P., Ern, M., Eckermann, S. D., & Riese, M. (2014). Differences in gravity wave drag between realistic oblique and assumed vertical propagation. *Journal of Geophysical Research: Atmospheres*, *119*, 10081–10099. https://doi.org/10.1002/2014JD021779

Kidston, J., Scaife, A. A., Hardiman, S. C., Mitchell, D. M., Butchart, N., Baldwin, M. P., & Gray, L. J. (2015). Stratospheric influence on tropospheric jet streams, storm tracks and surface weather. *Nature Geoscience*, *8*(6), 433–440. https://doi.org/10.1038/ngeo2424

Kim, Y. H., Bushell, A. C., Jackson, D. R., & Chun, H.-Y. (2013). Impacts of introducing a convective gravity-wave parameterization upon the QBO in the met office unified model. *Geophysical Research Letters*, *40*(9), 1873–1877. https://doi.org/10.1002/grl.50353

Kim, Y.-J., Eckermann, S. D., & Chun, H.-Y. (2003). An overview of the past, present, and future of gravity-wave drag parameterization for numerical climate and weather prediction models. *Atmosphere-Ocean*, *41*(1), 65–98. https://doi.org/10.3137/ao.410105

Koch, S. E., & Siedlarz, L. M. (1999). Mesoscale gravity waves and their environment in the central United States during STORM-FEST. *Monthly Weather Review*, *127*(12), 2854–2879. https://doi.org/10.1175/1520-0493(1999)127<2854:mgwate>2.0.co;2

Krasauskas, L., Kaifler, B., & Ungermann, J. (2022). GLORIA 3-D temperature and ALIMA temperature measurements from flight 12 of the SouthTRAC measurement campaign [Dataset]. Zenodo. https://doi.org/10.5281/zenodo.7155729

Krasauskas, L., Ungermann, J., Ensmann, S., Krisch, I., Kretschmer, E., Preusse, P., & Riese, M. (2019). 3-D tomographic limb sounder retrieval techniques: Irregular grids and laplacian regularisation. *Atmospheric Measurement Techniques*, *12*(2), 853–872. https://doi.org/10.5194/amt-12-853-2019

Krasauskas, L., Ungermann, J., Preusse, P., Friedl-Vallon, F., Zahn, A., Ziereis, H., et al. (2021). 3-D tomographic observations of Rossby wave breaking over the North Atlantic during the wise aircraft campaign in 2017. *Atmospheric Chemistry and Physics*, *21*(13), 10249–10272. https://doi.org/10.5194/acp-21-10249-2021

Krautstrunk, M., & Giez, A. (2012). The transition from FALCON to HALO era airborne atmospheric research. In U. Schumann (Ed.), *Atmospheric physics* (pp. 609–624). Springer Verlag. https://doi.org/10.1007/978-3-642-30183-4_37

Krisch, I., Ern, M., Hoffmann, L., Preusse, P., Strube, C., Ungermann, J., & Riese, M. (2020). Superposition of gravity waves with different propagation characteristics observed by airborne and space-borne infrared sounders. *Atmospheric Chemistry and Physics*, *20*(19), 11469–11490. https://doi.org/10.5194/acp-20-11469-2020

Krisch, I., Preusse, P., Ungermann, J., Dörnbrack, A., Eckermann, S. D., Ern, M., et al. (2017). First tomographic observations of gravity waves by the infrared limb imager GLORIA. *Atmospheric Chemistry and Physics*, *17*(24), 14937–14953. https://doi.org/10.5194/acp-17-14937-2017

Krisch, I., Ungermann, J., Preusse, P., Kretschmer, E., & Riese, M. (2018). Limited angle tomography of mesoscale gravity waves by the infrared limb-sounder GLORIA. *Atmospheric Measurement Techniques*, *11*(7), 4327–4344. https://doi.org/10.5194/amt-11-4327-2018

Lehmann, C. I., Kim, Y.-H., Preusse, P., Chun, H.-Y., Ern, M., & Kim, S.-Y. (2012). Consistency between Fourier transform and small-volume few-wave decomposition for spectral and spatial variability of gravity waves above a typhoon. *Atmospheric Measurement Techniques*, *5*(7), 1637–1651. https://doi.org/10.5194/amt-5-1637-2012

Lighthill, M. J. (1978). *Waves in fluids* (p. 504). Cambridge University Press.

Lott, F., & Miller, M. J. (1997). A new subgrid scale orographic drag parameterization: Its formulation and testing. *Quarterly Journal of the Royal Meteorological Society*, *123*(537), 101–127. https://doi.org/10.1002/qj.49712353704

Lu, X., Chen, C., Huang, W., Smith, J. A., Chu, X., Yuan, T., et al. (2015). A coordinated study of 1 hr mesoscale gravity waves propagating from logan to boulder with CRRL Na Doppler lidars and temperature mapper. *Journal of Geophysical Research: Atmospheres*, *120*(19), 10006–10021. https://doi.org/10.1002/2015JD023604

Marks, C. J., & Eckermann, S. D. (1995). A three-dimensional non-hydrostatic ray-tracing model for gravity waves: Formulation and preliminary results for the middle atmosphere. *Journal of the Atmospheric Sciences*, *52*(11), 1959–1984. https://doi.org/10.1175/1520-0469(1995)052⟨1959:ATDNRT⟩2.0.CO;2

Marquardt, D. W. (1963). An algorithm for least squares estimation of nonlinear parameters. *Journal of the Society for Industrial and Applied Mathematics*, *11*(2), 431–441. https://doi.org/10.1137/0111030

McLandress, C. (1998). On the importance of gravity waves in the middle atmosphere and their parameterization in general circulation models. *Journal of Atmospheric and Solar-Terrestrial Physics*, *60*(14), 1357–1383. https://doi.org/10.1016/S1364-6826(98)00061-3

McLandress, C., Shepherd, T. G., Polavarapu, S., & Beagley, S. R. (2012). Is missing orographic gravity wave drag near 60°S the cause of the stratospheric zonal wind biases in chemistry climate models? *Journal of the Atmospheric Sciences*, *69*(3), 802–818. https://doi.org/10.1175/JAS-D-11-0159.1

Minamihara, Y., Sato, K., & Tsutsumi, M. (2020). Intermittency of gravity waves in the Antarctic troposphere and lower stratosphere revealed by the pansy radar observation. *Journal of Geophysical Research: Atmospheres*, *125*(15), e2020JD032543. https://doi.org/10.1029/2020JD032543

Morlet, J., Arens, G., Fourgeau, E., & Glard, D. (1982). Wave propagation and sampling theory—Part I: Complex signal and scattering in multilayered media. *GEOPHYSICS*, *47*(2), 203–221. https://doi.org/10.1190/1.1441328

Nastrom, G., Fritts, D., & Gage, K. (1987). An investigation of terrain effects on the mesoscale spectrum of atmospheric motions. *Journal of the Atmospheric Sciences*, *44*(20), 3087–3096. https://doi.org/10.1175/1520-0469(1987)044⟨3087:AIOTEO⟩2.0.CO;2

National Geophysical Data Center. (2009). *ETOPO1 arc-minute global relief model*. NOAA National Centers for Environmental Information. Retrieved from https://www.ngdc.noaa.gov/mgg/global/

O'Sullivan, D., & Dunkerton, T. J. (1995). Generation of inertia-gravity waves in a simulated life cycle of baroclinic instability. *Journal of Atmospheric Sciences*, *52*(21), 3695–3716. https://doi.org/10.1175/1520-0469(1995)052⟨3695:GOIWIA⟩2.0.CO;2

Palmer, T. N., Shutts, G. J., & Swinbank, R. (1986). Alleviation of a systematic westerly bias in general circulation and numerical weather prediction models through an orographic gravity wave drag parameterization. *Quarterly Journal of the Royal Meteorological Society*, *112*(474), 1001–1093. https://doi.org/10.1002/qj.49711247406

Perrett, J. A., Wright, C. J., Hindley, N. P., Hoffmann, L., Mitchell, N. J., Preusse, P., & Eckermann, S. D. (2021). Determining gravity wave sources and propagation in the Southern Hemisphere by ray-tracing AIRS measurements. *Geophysical Research Letters*, *48*(2), e2020GL088621. https://doi.org/10.1029/2020GL088621

Plougonven, R., dela Camara, A., Hertzog, A., & Lott, F. (2020). How does knowledge of atmospheric gravity waves guide their parameterizations? *Quarterly Journal of the Royal Meteorological Society*, *146*(728), 1529–1543. https://doi.org/10.1002/qj.3732

Plougonven, R., & Zhang, F. (2014). Internal gravity waves from atmospheric jets and fronts. *Reviews of Geophysics*, *52*(1), 33–76. https://doi.org/10.1002/2012RG000419

Podglajen, A., Hertzog, A., Plougonven, R., & Legras, B. (2016). Lagrangian temperature and vertical velocity fluctuations due to gravity waves in the lower stratosphere. *Geophysical Research Letters*, *43*(7), 3543–3553. https://doi.org/10.1002/2016GL068148

Polichtchouk, I., Shepherd, T. G., Hogan, R. J., & Bechtold, P. (2018). Sensitivity of the Brewer-Dobson circulation and polar vortex variability to parameterized nonorographic gravity wave drag in a high-resolution atmospheric model. *Journal of the Atmospheric Sciences*, *75*(5), 1525–1543. https://doi.org/10.1175/JAS-D-17-0304.1

Pramitha, M., Venkat Ratnam, M., Taori, A., Krishna Murthy, B. V., Pallamraju, D., & Vijaya Bhaskar Rao, S. (2015). Evidence for tropospheric wind shear excitation of high-phase-speed gravity waves reaching the mesosphere using the ray-tracing technique. *Atmospheric Chemistry and Physics*, *15*(5), 2709–2721. https://doi.org/10.5194/acp-15-2709-2015

Preusse, P., Eckermann, S. D., Ern, M., Oberheide, J., Picard, R. H., Roble, R. G., et al. (2009). Global ray-tracing simulations of the SABER gravity wave climatology. *Journal of Geophysical Research*, *114*(D8), D08126. https://doi.org/10.1029/2008JD011214

Preusse, P., Hoffmann, L., Lehmann, C., Alexander, M. J., Broutman, D., Chun, H.-Y., & Vial, F. (2012). Observation of gravity waves from space (p. 195). Final report, ESA study, CN/22561/09/NL/AF.

Ralph, F., Neiman, P., & Keller, T. (1999). Deep-tropospheric gravity waves created by leeside cold fronts. *Journal of the Atmospheric Sciences*, *56*, 2986–3009. https://doi.org/10.1175/1520-0469(1999)056⟨2986:DTGWCB⟩2.0.CO;2

Rao, J., Garfinkel, C. I., White, I. P., & Schwartz, C. (2020). The Southern Hemisphere minor sudden stratospheric warming in September 2019 and its predictions in S2S models. *Journal of Geophysical Research: Atmospheres*, *125*(14), e2020JD032723. https://doi.org/10.1029/2020JD032723

Rapp, M., Kaifler, B., Dörnbrack, A., Gisinger, S., Mixa, T., Reichert, R., et al. (2021). SOUTHTRAC-GW: An airborne field campaign to explore gravity wave dynamics at the world's strongest hotspot. *Bulletin of the American Meteorological Society*, *102*(4), E871–E893. https://doi.org/10.1175/BAMS-D-20-0034.1

Riese, M., Friedl-Vallon, F., Spang, R., Preusse, P., Schiller, C., Hoffmann, L., et al. (2005). GLObal limb Radiance Imager for the Atmosphere (GLORIA): Scientific objectives. *Advances in Space Research*, *36*(5), 989–995. https://doi.org/10.1016/j.asr.2005.04.115

Russell, J. M., III, Mlynczak, M. G., Gordley, L. L., Tansock, J. J., Jr., & Esplin, R. W. (1999). Overview of the SABER experiment and preliminary calibration results. *Proceedings of SPIE*, *3756*, 277–288. https://doi.org/10.1117/12.366382

Sato, K. (1993). Small-scale wind disturbances observed by the MU radar during the passage of Typhoon Kelly. *Journal of the Atmospheric Sciences*, *50*(4), 518–537. https://doi.org/10.1175/1520-0469(1993)050<0518:sswdob>2.0.co;2

Sato, K., Watanabe, S., Kawatani, Y., Tomikawa, Y., Miyazaki, K., & Takahashi, M. (2009). On the origins of mesospheric gravity waves. *Geophysical Research Letters*, *36*(19), L19801. https://doi.org/10.1029/2009GL039908

Sato, K., Yamamori, M., Ogino, S. Y., Takahashi, N., Tomikawa, Y., & Yamanouchi, T. (2003). A meridional scan of the stratospheric gravity wavefield over the ocean in 2001 (MeSSO2001). *Journal of Geophysical Research*, *108*(4491), ACL31–ACL313. https://doi.org/10.1029/2002JD003219

Savitzky, A., & Golay, M. J. E. (1964). Smoothing and differentiation of data by simplified least squares procedures. *Analytical Chemistry*, *36*(8), 1627–1639. https://doi.org/10.1021/ac60214a047

Scinocca, J. F., & McFarlane, N. A. (2000). The parametrization of drag induced by stratified flow over anisotropic orography. *Quarterly Journal of the Royal Meteorological Society*, *126*(568), 2353–2393. https://doi.org/10.1002/qj.49712656802

Scinocca, J. F., McFarlane, N. A., Lazare, M., Li, J., & Plummer, D. (2008). Technical note: The CCCma third generation AGCM and its extension into the middle atmosphere. *Atmospheric Chemistry and Physics*, *8*(23), 7055–7074. https://doi.org/10.5194/acp-8-7055-2008

Shapiro, L. G., & Stockman, G. C. (2001). *Computer vision* (Vol. 3). Prentice Hall.

Smith, R. B., Nugent, A. D., Kruse, C. G., Fritts, D. C., Doyle, J. D., Eckermann, S. D., et al. (2016). Stratospheric gravity wave fluxes and scales during DEEPWAVE. *Journal of the Atmospheric Sciences*, *73*(7), 2851–2869. https://doi.org/10.1175/JAS-D-15-0324.1

Stober, G., Sommer, S., Rapp, M., & Latteck, R. (2013). Investigation of gravity waves using horizontally resolved radial velocity measurements. *Atmospheric Measurement Techniques*, *6*(10), 2893–2905. https://doi.org/10.5194/amt-6-2893-2013

Strube, C., Preusse, P., Ern, M., & Riese, M. (2021). Propagation paths and source distributions of resolved gravity waves in ECMWF-IFS analysis fields around the southern polar night jet. *Atmospheric Chemistry Physics*, *21*(24), 18641–18668. https://doi.org/10.5194/acp-21-18641-2021

Thurairajah, B., & Cullens, C. Y. (2022). On the downward progression of stratospheric temperature anomalies using long-term SABER observations. *Journal of Geophysical Research: Atmospheres*, *127*(11). https://doi.org/10.1029/2022JD036487

Torrence, C., & Compo, G. P. (1998). A practical guide to wavelet analysis. *Bulletin of the American Meteorological Society*, *79*(1), 61–78. https://doi.org/10.1175/1520-0477(1998)079⟨0061:APGTWA⟩2.0.CO;2

Trinh, Q. T., Kalisch, S., Preusse, P., Ern, M., Chun, H.-Y., Eckermann, S. D., & Riese, M. (2016). Tuning of a convective gravity wave source scheme based on HIRDLS observations. *Atmospheric Chemistry and Physics*, *16*(11), 7335–7356. https://doi.org/10.5194/acp-16-7335-2016

Ungermann, J., Blank, J., Lotz, J., Leppkes, K., Hoffmann, L., Guggenmoser, T., et al. (2011). A 3-D tomographic retrieval approach with advection compensation for the air-borne limb-imager GLORIA. *Atmospheric Measurement Techniques*, *4*(11), 2509–2529. https://doi.org/10.5194/amt-4-2509-2011

Ungermann, J., Hoffmann, L., Preusse, P., Kaufmann, M., & Riese, M. (2010). Tomographic retrieval approach for mesoscale gravity wave observations by the PREMIER infrared limb-sounder. *Atmospheric Measurement Techniques*, *3*(2), 339–354. https://doi.org/10.5194/amt-3-339-2010

Ungermann, J., Kaufmann, M., Hoffmann, L., Preusse, P., Oelhaf, H., Friedl-Vallon, F., & Riese, M. (2010). Towards a 3-D tomographic retrieval for the air-borne limb-imager GLORIA. *Atmospheric Measurement Techniques*, *3*(6), 1647–1665. https://doi.org/10.5194/amt-3-1647-2010

van Niekerk, A., & Vosper, S. (2021). Towards a more "scale-aware" orographic gravity wave drag parametrization: Description and initial testing. *Quarterly Journal of the Royal Meteorological Society*, *147*(739), 3243–3262. https://doi.org/10.1002/qj.4126

Vincent, R., & Alexander, M. (2000). Gravity waves in the tropical lower stratosphere: An observational study of seasonal and interannual variability. *Journal of Geophysical Research*, *105*(D14), 17971–17982. https://doi.org/10.1029/2000JD900196

Wagner, J., Doernbrack, A., Rapp, M., Gisinger, S., Ehard, B., Bramberger, M., et al. (2017). Observed versus simulated mountain waves over Scandinavia-improvement of vertical winds, energy, and momentum fluxes by enhanced model resolution? *Atmospheric Chemistry and Physics*, *17*(6), 4031–4052. https://doi.org/10.5194/acp-17-4031-2017

Weinreb, M. P., & Neuendorffer, A. C. (1973). Method to apply homogeneous-path transmittance models to inhomogeneous atmospheres. *Journal of the Atmospheric Sciences*, *30*, 662–666. https://doi.org/10.1175/1520-0469(1973)030⟨0662:MTAHPT⟩2.0.CO;2

Worthington, R. M. (1999). Alignment of mountain wave patterns above wales: A VHF radar study during 1990–1998. *Journal of Geophysical Research*, *104*(D8), 9199–9212. https://doi.org/10.1029/1999jd900054

Wrasse, C. M., Nakamura, T., Takahashi, H., Medeiros, A. F., Taylor, M. J., Gobbi, D., et al. (2006). Mesospheric gravity waves observed near-equatorial and low-middle latitude stations: Wave characteristics and reverse ray-tracing results. *Annales Geophysicae*, *24*(12), 3229–3240. https://doi.org/10.5194/angeo-24-3229-2006